

Hydrogen plasmas with ICRF inverted minority and mode conversion heating regimes in the JET tokamak*

M.-L. Mayoral¹, P.U. Lamalle², D. Van Eester², E. A. Lerche², P. Beaumont¹, E. De La Luna³, P. De Vries¹, C. Gowers¹, R. Felton¹, J. Harling¹, V. Kiptily¹, K. Lawson¹, M. Laxåback⁴, P. Lomas¹, M.J. Mantsinen⁵, F. Meo⁶, J.-M. Noterdaeme^{7,8}, I. Nunes⁹, G. Piazza¹⁰, M. Santala⁵ and JET EFDA contributors**

1 Euratom/UKAEA Fusion Association, Culham Science Centre, Abingdon, Oxon, OX14 3DB, U.K.

2 Association Euratom-Belgian State, LPP-ERM/KMS, Partner in TEC, B-1000 Brussels, Belgium

3 Asociación Euratom-CIEMAT, Laboratorio Nacional de Fusión, Spain

4 Euratom-VR Association, Sweden

5 Helsinki U. of Technology, Tekes-Euratom Association, Finland

6 Association Euratom-RISO, Riso National Laboratory, Denmark

7 Max-Planck-Institut für Plasmaphysik, EURATOM-Assoziation, Germany

8 EESA Lab, University Gent, Belgium

9 Associação EURATOM/IST, Centro de Fusão Nuclear, Portugal

10 Forschungszentrum Karlsruhe (FZK), Germany

* This paper is an expanded version of material originally presented at 16th Topical Conference on Radio-Frequency in Plasmas, Park City, Utah, 11-13 April 2005. Proceedings edited by Stephen J. Wukitch and P.

Bonoli, American Institut of Physics, Melville, New-York, Vol. **787**, 122-128, 2005 and

<http://proceedings.aip.org/proceedings/confproceed/787.jsp>

** See the Appendix of J. Pamela *et al.*, in Fusion Energy 2004 (Proc. 20th Int. Conf. Vilamoura, 2004) (Vienna: IAEA) CD-ROM file OV/1-2 and <http://www-naweb.iaea.org/napc/physics/fec/fec2004/datasets/index.html>

PACS numbers: 52.50.Qt; 52.60.Qt

Short title: ICRF inverted minority and mode conversion regimes in JET

Abstract:

During the initial operation of the International Thermonuclear Experimental Reactor (ITER), it is envisaged that activation will be minimised by using hydrogen (H) plasmas where the reference ion cyclotron resonance frequency (ICRF) heating scenarios rely on minority species such as helium (^3He) or deuterium (D). This paper firstly describes experiments dedicated to the study of ^3He heating in H plasmas with a sequence of discharges in which 5 MW of ICRF power was reliably coupled and the ^3He concentration, controlled in real-time, was varied from below 1 % up to 10 %. The minority heating regime was observed at low concentrations (up to 2 %). Energetic tails in the ^3He ion distributions were observed with effective temperatures up to 300 keV and bulk electron temperatures up to 6 keV. At around 2 %, a sudden transition was reproducibly observed to the mode conversion regime, in which the ICRF fast wave couples to short wavelength modes, leading to efficient direct electron heating and bulk electron temperatures up to 8 keV. Secondly, experiments performed to study D minority ion heating in H plasmas are presented. This minority heating scheme proved much more difficult since modest quantities of carbon (C) impurity ions, which have the same charge to mass ratio as the D ions, led directly to the mode conversion regime. Finally, numerical simulations to interpret these two sets of experiments are under way and preliminary results are shown.

(Figures in this article are in colour only in the electronic version)

1 Introduction

It is envisaged that, in the initial phase of International Thermonuclear Experimental Reactor (ITER) [1] operation, H plasmas will be used to minimise the activation of the machine during the commissioning stages. The two relevant ICRF scenarios foreseen in H plasmas are based on the heating of ^3He minority ions, referred to as (^3He)H, or D minority ions, referred to as (D)H. A key feature of these so-called inverted scenarios is that the minority ion species have a smaller charge to mass ratio than the majority ion species, i.e. $Z_{\min}/A_{\min} < Z_{\text{maj}}/A_{\text{maj}}$. In the past, tritium (T) inverted scenarios in D plasmas with T and D fractions of 5 % and 95 % respectively, have been successfully tested during the 1997 JET DT campaign [2]. Further results were also obtained in the recent “Trace Tritium Experiment (TTE)” at JET [3], with tritium concentrations up to around 3.5 %. Nevertheless, until now (^3He)H and (D)H scenarios were only scarcely documented.

ICRF heating commonly relies on the propagation of the fast magnetosonic wave (in short, fast wave (FW)) to transport energy from the plasma edge to the core. The FW dispersion relation in the cold plasma approximation can be written as:

$$n_{\perp}^2 = \frac{[L - n_{\parallel}^2][R - n_{\parallel}^2]}{[S - n_{\parallel}^2]},$$

where R, L and S are the dielectric tensor components as defined by Stix [5]; $n_{\perp} = k_{\perp}c/\omega$ is the refractive index perpendicular to the equilibrium magnetic field, k_{\perp} is the perpendicular wave number; $n_{\parallel} = k_{\parallel}c/\omega$ is the refractive index parallel to the equilibrium magnetic field, k_{\parallel} is the parallel wave number. The FW propagation is illustrated in Figure 1 for plasma with two ion species. Two heating scenarios are shown: an inverted one (^3He)H and a standard one (^3He)D. The FW cut-offs are found for $n_{\parallel}^2 = R$ and $n_{\parallel}^2 = L$ (respectively associated with the

right- and left- handed wave polarisations). The cold FW resonance occurs for $n_{||}^2 = S$, which corresponds to the ion-ion hybrid resonance layer R_{ii} for a plasma with two ion species [6].

The mode conversion (MC) regime occurs if the FW incoming from the low magnetic field side (LFS) efficiently tunnels through the thin evanescence layer between the left-hand cut-off and the ion-ion hybrid layer. Then, considering a finite temperature plasma, the FW can be mode converted to hot plasma waves near the ion-ion hybrid layer. The nature of these short wavelength waves depends on the plasma properties [7]. They can be kinetic Alfvén waves, ion Bernstein waves (IBW) or electromagnetic ion cyclotron waves (ICW), depending on the relative importance of temperature and poloidal field effects [8][9][10]. Their main common characteristic is that they are strongly damped by electron Landau damping (ELD) because of the strong up- or down- shift of $k_{||}$ due to the presence of a finite poloidal magnetic field [11].

The minority heating (MH) regime occurs when the FW energy is dominantly absorbed at the ion cyclotron resonance layer R_{ic} . The minority ion cyclotron resonance condition can be written as $\omega_{ICRF} - n\omega_{c_i} - k_{||}v_{||} = 0$, where ω_{ICRF} is the ICRF wave frequency; ω_{c_i} is the minority ion cyclotron frequency; n is the harmonic number and $v_{||}$ is the minority ion parallel velocity. In this regime, the FW absorption by the minority ions results in the formation of a high-energy population, i.e. the appearance of a tail in the minority ion distribution function. The heating of the background ions and electrons takes place on the rather long time scale of the minority fast ions collisional slowing-down time (typically of the order of 0.4 s for the ^3He ions in the experiments described in this paper). When the energy of the fast minority ions is above a certain critical energy E_{crit} [5], the electrons are predominantly heated by collisions with the fast ions, whereas in the opposite case mainly ion heating is obtained.

In standard scenarios with $Z_{\min}/A_{\min} > Z_{\text{maj}}/A_{\text{maj}}$, the ion-ion hybrid layer R_{ii} is located on the high field side (HFS) of the minority ion cyclotron resonance layer R_{ic} . In that case, the FW launched from the LFS antennas encounters the minority ion cyclotron resonance layer first. MH is the main heating scenario unless the minority concentration exceeds a critical value above which the fast wave electric field component E_+ , which rotates in the same direction as the minority ions, is significantly reduced at the minority ion cyclotron layer. In the latter case, single-pass minority ion cyclotron damping decreases significantly, and a larger fraction of the FW can be mode-converted at the ion-ion hybrid layer. In JET, optimal concentration for the MC regime in D plasmas with ^3He ions was found in the range of 12-20% [12].

In inverted scenarios, the cold plasma theory places the ion-ion hybrid layer R_{ii} and the associated left-hand cut-off $R_{Lcut-off}$ between the minority ion cyclotron resonance R_{ic} and the LFS antenna [13] [14] (see illustration on Figure 1a), with R_{ii} moving to the LFS when the minority ion concentration is increased. In this case it is not immediately obvious which will be the preferential heating regime. Above a certain minority ion concentration, when the MH regime single-pass damping is very weak, the MC regime is expected to dominate. In particular, for high minority ion concentration ($> 20\%$), and if the plasma configuration is chosen in such a way that the minority ion cyclotron resonance is not located in the plasma, it has been shown on various tokamaks that efficient MC heating could be obtained [15][16]. Nevertheless, at very low minority ion concentration, when R_{ic} and R_{ii} are near each other, it is not obvious whether the FW will be dominantly mode converted or absorbed by the minority ion population. Indeed, even if R_{ii} is first encountered by the FW, the MH regime can occur if the minority ions have a temperature sufficiently high to Doppler broaden R_{ic} beyond of the left-hand wave cut-off.

Section 2 reports on ICRF heating experiments performed in H plasmas in which the ^3He concentration was scanned from 0.5 % to 10 %. The minority heating regime obtained for concentrations below 2 % as well as the transition to the mode conversion regime are studied. Section 3 reports on ICRF heating experiments with D minority ions in H plasmas. The strong influence of carbon impurity ions in this scheme is highlighted. Note that a concise summary of these two sets of experiments has been given in [4]. Finally, preliminary results from numerical simulations of these two heating schemes with the 1-D code TOMCAT and the 2-D full-wave code CYRANO are presented in section 4.

2 ICRF heating of H plasmas with ^3He Minority ions

2.1 Experimental set-up.

The experiments were carried out in H plasmas (with a small concentration of D from wall recycling (n_D/n_e) estimated of the order of 1-2 %) in the JET single-null divertor configuration with the following parameters: minor radius of 0.9 m, major radius of the magnetic axis around 3 m, toroidal vacuum magnetic field at 2.96 m (B_t) of 3.6 T, plasma current (I_p) of 2 MA and central electron density (n_{e0}) around $3 \cdot 10^{19} \text{ m}^{-3}$.

As discussed in the introduction, the ^3He concentration is one of the critical parameters influencing the FW damping. Hence its control and determination was crucial for these experiments. As ^3He gas is lost through transport, keeping the concentration at a specific level requires ^3He gas to be injected into the machine during the discharge [12]. A very efficient way to do this is to use the JET real-time central controller (RTCC) in order to link a measurement of the ^3He density to the opening of the gas injection valve. This technique, developed in the last few years [17], has been successfully used in the experiments presented here to control the ^3He concentration down to levels as low as 1.8 %. The ^3He concentration ($n_{^3\text{He}}/n_e$) was estimated from the effective charge of the ions and the relative concentration

of the majority and minority ions measured using the respective characteristic light emission in the divertor. Iron, argon, nickel, oxygen and carbon impurities were taken into account through the radiation spectrometer data. It should be noted that when a very low ^3He concentration ($< 1\%$) was required, it was only necessary to inject ^3He before the ICRF heating phase.

Up to 5 MW of ICRF power (P_{ICRF}) was applied using the four JET A2 ICRF antennas [18] at a nominal frequency of 37 MHz, positioning the fundamental ^3He cyclotron resonance layer $R_{ic}(^3\text{He})$ near the plasma centre (see Figure 2). Each ICRF antenna is fed by four transmission lines with slightly different electrical lengths connected to one generator. The four antennas are operated at slightly different frequencies around the nominal one in order to prevent cross-talk between generators, and also because small frequency variations are used in combination with line stretcher and stub adjustments in the ICRF system matching algorithm [19]. The exact frequencies used are summarised in Table 1 together with the corresponding ^3He cyclotron resonance major radii. In particular, because the frequency of antenna D differs significantly from the other three, a spread of about 10 cm is obtained in the resonance positions. Dipole phasing of the ICRF antennas was used to launch waves with a symmetric toroidal mode number (n_ϕ) spectrum and with $|n_\phi| \approx 27$ at the maximum of the antenna power spectrum. Asymmetric toroidal mode number spectra with $|n_\phi| \approx 14$ at the maximum of the antenna power spectrum were obtained with the $+90^\circ$ antenna phasing (predominantly in the co-current direction) and -90° antenna phasing (launched wave predominantly in the counter-current direction).

In all these pulses 1.3 MW of H neutral beam injection (NBI) was added in order to allow measurements of ion temperature profiles using the edge charge-exchange diagnostic (the charge exchange diagnostic viewing the plasma core was not available for the experiments described).

In order to experimentally deduce the electron power deposition profiles, the electron temperature response to an ICRF power modulation was analysed using a Fast Fourier Transform (FFT) technique (used to study the response of a system to a periodic perturbation) and Break-In-Slope (BIS) methods (which only requires a step change in the power level to estimate the absorption profiles) [17][20][21]. ICRF power was modulated during a 0.5 s period at the beginning and at the end of the ICRF power flat-top with a frequency of 20 Hz and an amplitude of 50 % (see example on Figure 3). The modulation period $\tau_{\text{mod}} = 0.05$ s, was chosen much smaller than the energy confinement time τ_E (typically of the order of 0.2 s in the experiment described in this paper) to ensure that the diffusion processes occur on a much longer time scale than τ_{mod} . This allows the straightforward application of the BIS analysis on the ECE signals for estimating the power deposition profiles.

The electron temperature T_e was measured using an electron cyclotron emission (ECE) heterodyne radiometer [22] with the number of channels recently increased to 96 in order to cover approximately the full plasma radius. The time resolution varies from 0.2 ms to 1 ms, the estimated radial resolution for each individual channel is around 2-5 cm and the separation between channels lower than 1 cm. Ever since the installation of the divertor, the centre of JET plasmas have been displaced vertically with respect to the equatorial plane of the tokamak. As a consequence, the ECE line of sight (located about 0.13 m above the machine midplane) passes below the magnetic axis by about 0.17 m (cf. Figure 2). When doing FFT and BIS analysis, two radial co-ordinates were available for data interpretation:

- The actual major radius position at which the measurements are made.
- The major radius position corresponding to the intersection of the magnetic surface on which the measurements are made, with the horizontal plane passing through the magnetic axis.

The second of these co-ordinates were used for the electron power deposition profiles presented in this paper as it illustrates the fact that the plasma core is not diagnosed, thus avoiding misinterpretation of the data. Moreover, as fast time evolution of the density profiles were not available, it was assumed that this quantity did not respond to the rapid changes of the modulated ICRF power. The total fraction of the ICRF power damped directly on electrons was estimated by integrating the electron power density profiles derived from the measurements over the plasma volume. For both FFT and BIS methods, it was assumed that transport processes occur on a time scale much longer than the modulation period [22][23]. Finally, information on the presence of fast ICRF-accelerated ions was obtained with gamma-ray (γ -ray) spectrometry analysis [24] and both low- and high-energy neutral particle analysis (NPA)[25].

2.2 ^3He minority heating regime in H plasmas

To establish the feasibility of ^3He MH regime in inverted scenarios a set of discharges was obtained with ^3He concentration below 2 %. Figure 3 shows an overview of three discharges with $n_{^3\text{He}} / n_e < 1$ % and different phasings of the ICRF antennas: dipole, $+90^\circ$ and -90° . In these pulses, the electron temperature increase, the production of neutrons and the gamma-rays emission indicated that a fast ^3He population was created and that ^3He MH regime was obtained. A maximum electron temperature T_e^{max} of 6.2 keV was reached with $+90^\circ$ phasing and $P_{\text{ICRF}} = 5$ MW. Central ion temperature measurements were not available for these experiments. Nevertheless, as illustrated in Figure 4, X-ray crystal spectrometer data were collected at a major radius $R = 3.25$ m giving an ion temperature, $T_i(3.25 \text{ m}) \approx 2$ keV to be compared with an electron temperature at the same location of $T_e(3.25 \text{ m}) \approx 3.4$ keV. Assuming standard L-mode profiles, one can then conclude that mainly electron heating was obtained with $T_i < T_e$.

The presence of a fast ^3He ion population led to an increase of the neutron rate (R_{NT}) which, in H plasmas, results from the nuclear reaction between the beryllium impurities and ^3He ions with energy above 0.9 MeV, i.e. $^9\text{Be}(^3\text{He},n)^{11}\text{C}$. A much higher neutron rate was obtained for the pulse 63313 (+90° phasing) indicating a higher energy ^3He population compared to pulses 63312 (dipole phasing) and 63314 (-90° phasing), which have similar ICRF power, ^3He concentration and electron density. The fast ^3He ion energy content (W_{fast}) defined as the perpendicular energy content in excess of twice the parallel value, i.e. $W_{fast} = W_{\perp} - 2W_{\parallel}$, was estimated as four thirds of the difference between the total plasma energy derived from diamagnetic loop measurements $W_{DIA} = 3/2W_{\perp}$, and the total plasma energy derived from magnetic calculations, $W_{MHD} = 3/4W_{\perp} + 3/2W_{\parallel}$, i.e. $W_{fast} = \frac{4}{3}(W_{DIA} - W_{MHD})$. This calculation gave a fast ^3He ion energy content up to 60 % higher in the +90° phasing case than in the -90° and dipole phasings cases.

More information on the fast ^3He ion population was obtained from the γ -rays produced by the nuclear reactions, firstly between ^3He ions with energy above 0.9 MeV and ^9Be impurity ions and secondly between ^3He ions with energy above 1.3 MeV and ^{12}C impurity ions [24]. The presence of a higher energy ^3He tail with +90° phasing was confirmed by the higher γ -ray emissivity (shown on Figure 5) for pulse 63313 than for pulses 63312 (dipole phasing) and 63314 (-90° phasing). In discharge 63319, also shown on Figure 5, the ^3He concentration was doubled with respect to discharge 63313. The increase by a factor of 1.7 in the γ -ray signal and neutron rate confirmed a higher fast ion population but with a lower temperature tail. In this pulse it was estimated that the tail temperature was $T_{tail} \approx 0.3 \pm 0.1 \text{ MeV}$.

The presence of ICRF accelerated ^3He ions was also illustrated by the R_{NT} , W_{DIA} and T_e^{\max} decrease (see Figure 3 and Figure 5) following the decrease of the averaged ICRF power during the ICRF power modulation between $t = 9 \text{ s}$ and $t = 9.4 \text{ s}$. High energy NPA confirmed

the existence of a fast ^3He population but the fluxes of ^3He ions were too small to make any definite conclusions on the ^3He distribution function.

Information on the radial profile of the fast ^3He population was obtained from γ -ray emission profiles measured with the JET neutron and γ -ray diagnostics [24], [26]. These consist of two cameras, vertical and horizontal, with nine and ten lines of sight, respectively. The line-integral measurements of the γ -ray emission along the lines of sight were tomographically reconstructed [27] in order to give the local γ -ray emissivity in a poloidal cross section, as shown in Figure 6. The results obtained were found in agreement with the past observations of the ICRF-induced orbit pinch effect in presence of toroidally directed waves [28][29][30]. In the $+90^\circ$ phasing case, the inward pinch of the resonant trapped ion orbits turning points leads to detrapping and produces a significant number of high-energy non-standard passing ions on the low field side of the resonance [31]. In the -90° phasing case, which corresponds to an ICRF-induced outward pinch, the standard trapped orbits dominate and the turning points of the orbits move outwards along the resonance layer leading to a narrower and more elongated γ -ray profile (see Figure 6).

It should be noted that in both pulses with $+90^\circ$ phasing (63313 and 63319), toroidal Alfvén eigenmodes (AEs) with frequencies between 220 and 260 kHz were observed during the ICRF power flat-top while in the pulses with dipole (63312) and -90° phasing (63314) such activity was not seen. Energetic ions can destabilise AEs with the drive proportional to the radial pressure gradient of the fast ions at the location of the mode when $n_\phi \omega_{fast} > \omega$. Here n_ϕ is the toroidal mode number; ω is the mode frequency and ω_{fast} is the fast ion diamagnetic frequency, which is proportional to the radial pressure gradient of the energetic ion distribution function and increases with the effective tail temperature [32]. This suggests that the pulses with $+90^\circ$ phasing ICRF waves generated fast ions with more peaked radial pressure profiles and tails with energies high enough to excite AEs.

2.3 Transition from ICRF minority heating to MC heating

As the ^3He concentration was increased above 2 % a reproducible transition from the MH to the MC regime was observed. This transition to a different heating regime was seen on several diagnostic signals. First, as $n_{^3\text{He}}/n_e$ was increased, the T_e response to the ICRF power modulation gradually changed, indicating a change in the power deposition characteristics. In Figure 7, the time evolution of T_e at R = 2.8 m and the ^3He concentration are plotted for pulse 63322 for which the ICRF modulation was applied throughout the ICRF power flat-top. One can clearly see a dramatic change in the T_e response as $n_{^3\text{He}}/n_e$ become larger than 2 % ($t \approx 8.2$ s). As discussed in the introduction, the finite slowing-down time of fast ions on the electrons in the MH regime leads to a delay in the temperature response with respect to the ICRF power modulation. In the MC regime, electron heating is a direct process by ELD. Indeed, one can see in Figure 7(b) that, for $n_{^3\text{He}}/n_e \approx 3.2$ %, the T_e response is in phase with the power modulation, consistent with dominant direct electron heating. For $n_{^3\text{He}}/n_e \approx 0.8$ % case (see Figure 7(a)), the period of the modulation of 0.05 s associated with an estimated fast ^3He slowing down time of about 0.4 s prevents us, as expected, from seeing any clear T_e response.

The decrease in T_e observed after the transition between the two heating schemes (from $t \approx 8.5$ s) indicates that the optimal conditions for efficient electron heating are different in the MC and MH regimes. In the following section we show results in which the experimental conditions were optimised for the MC regime.

The transition between MH and MC was further confirmed by the disappearance of the fast ^3He population for $n_{^3\text{He}}/n_e > 2$ %. This was seen on the γ -ray emission (requiring ^3He ions with energy above 0.9 MeV) shown in Figure 8 for the pulses 63319, 63320 and 63324, which differ only in ^3He concentration. In discharge 63319, a high signal was measured

throughout the pulse as the ^3He concentration stayed below 1.8 %. In discharge 63320, as $n_{^3\text{He}}/n_e$ was increased above 2 % for $t \approx 6.3$ s the γ -ray signal began to decrease to finally disappear. Almost no signal was collected in discharge 63324. One can also notice in Figure 8, the small decrease in ICRF power for pulse 63320 and the very ragged ICRF power for pulse 63324. This perturbation in the power was due to strong modification in the antenna loading as the ICRF wave absorption mechanism changed at the transition between the two regimes.

The 2 % threshold concentration was also confirmed by plotting the fast ions energy content for a large range of pulses with different ICRF phasing, total heating power and magnetic field as a function of the ^3He concentration (see Figure 9). It should be noted that additional experimental data would be required to document more precisely the heating regime transition between $n_{^3\text{He}}/n_e = 2$ % and $n_{^3\text{He}}/n_e = 2.5$ % and investigate the effect of the antenna phasing. Indeed, the width of the Doppler-shift-broadened ^3He absorption region as well as that of the evanescence layer between the ion-ion layer and the left-hand cut-off (and hence the conversion efficiency) depends on the parallel wave number $k_{\parallel} \sim |n_{\phi}|/R$ (with R the plasma major radius). Consequently, the critical minority concentration between the two regimes is expected to be different for different antenna phasings [33].

An estimate of the electron deposition profiles before and after the change of heating regime was obtained with a BIS analysis of the pulse 63322 (previously presented in Figure 7) for which the ICRF power modulation was applied throughout the ICRF flat-top. As mentioned in the introduction, the BIS profiles were mapped onto the equatorial plane of the plasma. This is illustrated on the poloidal sections presented in Figure 13, where one can see that no temperature measurements were available for major radius between 2.9 m and 3.1 m. Two electron deposition radial profiles are shown in Figure 10, corresponding to times preceding

and following the heating regime transition. These deposition profiles were obtained from an upgraded BIS method [34], in which the phase lags between the power modulation and the electron temperature response, that occur during indirect electron heating, are taken into account meaning that both indirect and direct electron deposition are deduced. For $n_{^3\text{He}} / n_e \approx 0.8 \%$, a broad profile was obtained which seems to peak towards the undiagnosed plasma centre. This is consistent with indirect central electron heating from the fast ^3He ions created at the ^3He cyclotron resonance layer $R_{ic} (^3\text{He}) \approx 2.94 - 3.06$ m. Nevertheless, the deposition profile obtained was too broad to come from this heating alone. In order to find an explanation, these electron deposition profiles were compared with the ones deduced from standard BIS and FFT analysis. The upgraded BIS and the FFT methods are expected to give similar results. The standard BIS method, which neglects any phase lag between the power modulation and the electron temperature response, gives only direct electron deposition. Consequently, inconsistencies between FFT, upgraded BIS and standard BIS analyses can be used as a diagnostic to indicate where indirect heating is taking place [22]. The three methods were thus compared and the resulting electron deposition profiles for $n_{^3\text{He}} / n_e \approx 0.8 \%$ are shown in Figure 11. Between $R = 3.0$ m and $R = 3.3$ m, the FFT analysis and the new BIS analysis agree but are both in disagreement with the standard BIS analysis, indicating indirect electron heating. From $R = 3.3$ m and on the LFS, the three methods agree, indicating dominant off-axis direct electron heating, peaked around 3.3 m. Direct electron heating near $R = 3.3 - 3.4$ m was also confirmed by the decrease in the time delays between the temperature response and the power modulation, obtained from the upgraded BIS method as a function of the major radius (Figure 12). A clear decrease in the time delay is found near $R = 3.3 - 3.4$ m. The reason for such off-axis direct electron heating was attributed to be the presence of C impurity ions in the plasma, which have the same charge to mass ratio as the D minority ions. Note that the concentration of others impurities with the same charge to mass ratio as the C

ions was negligible compared to the C concentration (n_C / n_e) estimated to be 2-3 %. As the D and C ions have together the same effect on the FW propagation as a much higher D concentration, a new ion-ion hybrid layer, noted (D,C)-H appeared in the plasma where the FW could be mode converted. In Figure 13(a) this new ion-ion hybrid layer is represented in the case of 2 % of C and 2 % of D in a H plasma, with an additional 0.8% of ^3He . The resulting direct absorption on the electrons at $R \approx 2.6$ m was then observed on the same flux surface LFS at $R \approx 3.3$ m. The integrated power absorbed by the electrons was estimated to be 22 % and 32 % of the total ICRF power from the standard and the new BIS methods respectively. Simulations presented in section 4 of this paper will also confirm the presence of the (D,C)-H hybrid layer and its influence.

For a higher ^3He concentration $n_{^3\text{He}} / n_e \approx 2.6$ %, the electron power deposition profile (Figure 10 and Figure 13b) was much more peaked and located at a major radius around 3.15 m, in agreement with the location of the ^3He -H hybrid layer associated with 2.6% of ^3He in a H plasma. The integrated power transferred to the electrons was estimated to be 60 %, 69 % and 71 % of the total ICRF power from the standard BIS, the FFT and the new BIS methods respectively.

2.4 Mode conversion regime in H plasmas

In order to further investigate the MC regime, experiments were performed with a magnetic field lowered to 3.3 T and a ^3He concentration of 3.5 %. The resulting ^3He -H hybrid layer was located at a major radius $R \approx 2.8$ m instead of $R \approx 3.15$ m in the previously discussed pulses. NBI power and therefore T_i measurements were not available for these pulses. An overview of the results obtained is presented in Figure 14 for dipole and +90° phasings. One can see that almost no neutrons were produced, which means that only a few, if any, fast ^3He ions with energy above 0.9 MeV were present. For the same reason, no γ -ray signal was collected.

Furthermore the NPA diagnostic, confirmed that no fast ^3He ions with energy above 400 keV, were produced during its time window of measurements i.e. 6 s to 9 s. Finally, the highest electron temperature, up to 8.5 keV, was obtained with 5 MW of ICRF power in the dipole case.

Radial profiles of the ICRF power density directly absorbed by the electron were deduced from BIS and FFT analysis of the temperature response to the ICRF modulation between 5.8 s and 6 s. The profiles from the upgraded BIS are shown Figure 15 (similar profiles were obtained with the standard BIS and FFT methods). They show an overall higher power density for the dipole phasing pulse (63384) than for the $+90^\circ$ phasing pulse (63383) with a total power integrated up to the plasma edge estimated about 82% to 63 % of the coupled ICRF power, respectively. One may question the quality of the ECE data near the plasma edge, hence the edge “bump” on the profiles of Figure 15. However the integrated power inside a normalised minor radius of 0.8 (62 % and 53 % of the ICRF coupled power) shows similar trend.

3 ICRF heating of D ions in H plasmas

The experimental set-up for these experiments was similar to the one described above. The experiments were carried out at a toroidal vacuum magnetic field at 2.96 m of 3.9 T, a plasma current of 2 MA and a central electron density of $3 \cdot 10^{19} \text{ m}^{-3}$. The D minority concentration resulted from D ion desorption from the wall, the legacy of previous D plasma operation, and was estimated to be $n_D/n_e = 1\text{-}2 \%$. In order to position the fundamental D cyclotron resonance in the plasma centre ($R \approx 3.1 \text{ m}$), ICRF waves at a nominal frequency of 29 MHz were used. The exact operating frequencies for the four antennas and the corresponding fundamental D cyclotron resonances are summarised in Table 2. Dipole phasing of the antennas was used.

An overview of a typical discharge is presented in Figure 16. The coupling of the ICRF power was very challenging in this set of experiments and only brief peaks at a maximum value of 2.5 MW were achieved. Most of the time the averaged coupled power was around 1.5 MW. The first reason for this power limitation comes from the fact that 29 MHz is near the limit of the generator capability. Secondly, the antenna coupling resistance was unusually low and unsteady indicating poor wave absorption.

Strikingly, no D fast ions were detected, either by the neutral particle analyser or the γ -ray emission. No neutrons were detected and the maximum electron temperature obtained was around 3 keV. BIS analysis performed on several pulses revealed, as illustrated in Figure 17, a rather peaked electron power deposition profile maximum at $R \approx 3.5$ m and with a full width at half maximum of around 30 cm. The total power absorbed by the electrons was estimated to be 50 % of the ICRF power. This off-axis electron heating could only be explained by the presence in the plasma of 2-3 % of C, leading directly to the mode conversion regime. The effect of 2 % of C on the dispersion relation is shown on Figure 18. On Figure 18(a) the dispersion relation is plotted with $n_D / n_e = 2$ % and in Figure 18(b) with $n_D / n_e = 2$ % and $n_C / n_e = 2$ %. When adding 2 % of C, the ion-ion hybrid layer R_{ii} is moved to the LFS at a major radius of around 3.5 m. The fast wave is then mode converted before reaching the D cyclotron resonance layer, preventing any D minority heating.

No optimisation of this mode conversion heating scheme was attempted mainly because lowering the magnetic field to position the mode conversion layer more centrally would have introduced the ^3He ion cyclotron resonance in the plasma.

4 Numerical simulations

Simulations have been performed with the 1-D code TOMCAT [35] and the 2-D full wave code CYRANO [36] to aid in the interpretation of the experimental results. TOMCAT is a finite element code based on a variational principle for studying one-dimensional fast wave

propagation and damping near the ion-ion hybrid conversion layer in tokamaks [35]. Finite Larmor radius (FLR) corrections up to second order in $\rho_L k_\perp$, where ρ_L is the Larmor radius, are taken into account in the expansions of the RF field and of the Galerkin test function components appearing in this formulation. This accounts for the fast and slow wave modes, as well as finite temperature modes. Toroidicity and oblique wave incidence effects are included; hence TOMCAT correctly describes the physics of 1-D conversion physics. However, the absorption of the mode converted wave is not adequately modelled because poloidal magnetic field effects are neglected. CYRANO is a 2-D full-wave code in toroidal geometry including the finite electron mass, FLR corrections up to second order in $\rho_L k_\perp$ and an accurate description of poloidal magnetic field effects, such as a specific k_\parallel for each poloidal RF field mode, and the resulting increase of electron Landau damping and TTMP for high poloidal mode numbers [36]. Maxwell's equations for the wave field are solved using Fourier series in the poloidal and toroidal directions and a finite element method. We stress that modelling mode conversion to short wave modes in two dimensions is a very challenging problem, the adequate treatment of which has recently started by appealing to massively parallel computers [37]. The CYRANO results presented here are accordingly preliminary for the MC regime, because our present computer capability only allows a partial numerical resolution of the short mode converted waves in the poloidal direction for a large tokamak such as JET. These simulations will be readdressed in a future paper as soon as adequate computer power becomes available to us.

4.1 Modelling of ICRF heating of H plasmas with ^3He Minority ions

CYRANO and TOMCAT simulations were performed with parameters matching the experiments described in section 2.3, i.e. a magnetic field at the magnetic axis of 3.6 T, a central electron density of $3 \cdot 10^{19} \text{ m}^{-3}$, an ICRF frequency of 37 MHz (resulting in a central

^3He ion cyclotron resonance) and several values of the ^3He concentration ($n_{^3\text{He}}/n_e$ between 0.5 % and 10 %). As expected the simulations reproduce a transition from dominant ^3He to dominant electron absorption as the ^3He concentration increases. The introduction in the simulations of D concentrations up to 2 %, representative of the experimental conditions, did not show any significant influence on the heating scenarios.

Next, maintaining the D concentration at 2 %, the ^3He concentration scan was repeated with carbon concentrations $n_C/n_e = 1\%$ and 2% . As discussed in section 2.3 the addition of small amounts of C introduces the (D,C)-H hybrid layer in the plasma. Note that any impurity with $Z/A = 1/2$ has a similar effect. The simulations show that the C impurity content of the plasma can indeed considerably influence the ICRF power absorption, in particular for very low ^3He concentrations in the MH regime. The relative power fractions absorbed by the electrons and the ^3He ions obtained by CYRANO for 0 % and 2 % of C (both with 2 % of D), are presented in Figure 19 for the dominant toroidal mode number of dipole phasing, $n_\varphi = -27$. If one considers that the transition between the MH and the MC regimes occurs when the absorption by the ^3He ions becomes smaller than the absorption by the electrons, one sees that in the absence of C the transition occurs for $n_{^3\text{He}}/n_e \approx 5\%$. As soon as C ions are included the ^3He level at which the transition occurs decreases. When $n_C/n_e = 1\%$ is assumed (not shown) the transition occurs at around $n_{^3\text{He}}/n_e \approx 4\%$. With $n_C/n_e = 2\%$, the transition occurs near $n_{^3\text{He}}/n_e \approx 3\%$, in better agreement with the value obtained in the experiments (for which the C concentration was estimated around 2-3 %). Similar transition levels have been obtained with TOMCAT. The fact that the ^3He level at which the transition occurs decreases when increasing the C concentration can be explained if one keeps in mind that the power absorbed by the electrons includes power from the mode converted waves associated with the ^3He -H hybrid resonance but also from the mode converted waves associated with the (D,C)-H hybrid

resonance (FW ELD/TTMP is found to be negligible in the present conditions). Note that because of the plasma quasi-neutrality, for a fixed ${}^3\text{He}$ concentration, the introduction of carbon ions decreases the H concentration and thus slightly increase the ratio $n_{3\text{He}}/n_{\text{H}}$. Nevertheless, the effect on the ${}^3\text{He}$ -H hybrid layer appears to be minor. In figure 19, for $n_{3\text{He}}/n_e = 0.5\%$ and without C, almost all the power is absorbed by the ${}^3\text{He}$ ions and none is directly absorbed by the electrons. When including 2% of C, 30% of the power goes to the electrons because of MC at the (D,C)-H hybrid layer. As a matter of fact, this parasitic direct electron heating was highlighted experimentally by the BIS analysis of the temperature response in the ${}^3\text{He}$ MH regime (see paragraph 2.3 and discussion of Figure 10).

Both codes show that when the C impurity is taken into account, the ${}^3\text{He}$ absorption is maximum for ${}^3\text{He}$ concentration $n_{3\text{He}}/n_e \sim 1.5\text{-}2.5\%$. The strong increase of electron absorption resulting from the introduction of 2% of C and from the associated MC at the (D,C)-H hybrid layer is observed for up to $n_{3\text{He}}/n_e \sim 5\%$. Above this concentration, there is no difference in the electron absorption with and without C, meaning that the fast wave is then mainly mode converted at the ${}^3\text{He}$ -H hybrid layer.

Further simulations were performed with TOMCAT in similar conditions as the MC experiments described in section 2.4, i.e. a magnetic field at the magnetic axis of 3.3 T, a central electron density of $3 \cdot 10^{19} \text{ m}^{-3}$, an ICRF frequency of 37 MHz (resulting in a HFS ${}^3\text{He}$ ion cyclotron resonance) and 2% of C ions. The power transferred to the electrons (P_e) and to the ${}^3\text{He}$ ions ($P_{3\text{He}}$) was compared for two ${}^3\text{He}$ concentrations (2% and 3.5%), three plasma target temperatures (3 keV, 5 keV and 8 keV) and two toroidal mode numbers ($n_\phi = 27$ and $n_\phi = 14$). The results are summarised in Table 3, which gives the power fractions associated with the FW launched on the LFS of the plasma and allowed to reflect once on the HFS cut-

off, i.e. double-pass absorption power fraction. For the lower ${}^3\text{He}$ concentration $n_{3\text{He}}/n_e = 2\%$, the power absorbed by the electrons P_e is interestingly higher for the toroidal mode number $n_\phi = 14$ corresponding to the $+90^\circ$ phasing than for $n_\phi = 27$ corresponding to the dipole phasing. In both cases, the absorbed power profiles show that MC at the ${}^3\text{He}$ -H hybrid layer is negligible and that the main reason for electron absorption is MC at the (D,C)-H hybrid layer. The more efficient conversion in the $+90^\circ$ case can be explained by the dispersion relation shown in Figure 20. One can see that for $n_\phi = 14$ (Figure 20b) the FW right-hand cut-off is on the HFS of the (D,C)-H hybrid layer $x((\text{D,C})\text{-H})$, allowing a more efficient mode conversion compared to the $n_\phi = 27$ case (Figure 20a) for which the FW has to tunnel through its right-hand cut-off before reaching $x((\text{D,C})\text{-H})$. For $n_{3\text{He}}/n_e = 3.5\%$, and plasma target temperatures of 3 and 5 keV, the power absorbed by the electrons is 35 to 40% higher for the dipole than for the $+90^\circ$ phasing. Moreover if in the dipole phasing case, this power is mainly due to MC at the ${}^3\text{He}$ -H hybrid layer, in the $+90^\circ$ case, the power absorbed by the electrons is equally due to MC at the (${}^3\text{He}$ -H) and (D,C)-H hybrid resonances. The higher MC efficiency at ${}^3\text{He}$ -H hybrid layer for dipole phasing is in agreement with the experimental data presented section 2.4. For $n_{3\text{He}}/n_e = 3.5\%$, and plasma target temperatures of 8 keV, one notices a significant increase in the double-pass absorption by the ${}^3\text{He}$ ions which goes from 10% with 5 keV to 45% with 8 keV and an associated decrease in the electron absorption from 72% to 43%.

4.2 Modelling ICRF heating of D ions in H plasmas

TOMCAT simulations were performed for the experimental conditions of section 3 (magnetic field of 2 MA, a central electron density of $3 \cdot 10^{19} \text{ m}^{-3}$, an ICRF frequency of 37 MHz) and a toroidal mode number $n_\phi \approx 27$ corresponding to the peaks of the antenna power spectrum of dipole phasing. For D concentration $n_D/n_e = 2\%$, a C concentration scan was performed with

$n_c / n_e = 0 \%$, 0.5% , 1% , 1.5% and 2% . The power fractions absorbed by the electrons and the D ions are shown in Figure 21 as a function of the C concentration. This results clearly illustrate the strong reduction of the D absorption obtained by adding $\sim 1 \%$ of carbon impurity ions to the 2% of D minority ions. The deleterious influence of even very small concentration of carbon for the (D)H heating scheme is thus manifest. However, in the experiments described in section 3.2, the power fraction absorbed by the electrons was estimated $\sim 50 \%$ of the total absorbed power whereas the 1-D simulations gives 100% . This difference is likely to be related to the modest to poor absorptivity of the scheme but cannot be explained in detail from 1-D simulations. As manifest from the low and very unsteady antenna coupling during the experiments, wave absorption was indeed quite poor, and the resulting global pattern of standing waves in the tokamak had strong influence on power deposition [38]. The high sensitivity of the absorption efficiency on the D and C content in the plasma and the lack of accuracy on their experimental concentrations renders the interpretation of this inverted scenario very delicate. The fate of power channelled onto short wavelength branches has to be carefully assessed, accounting for realistic profiles, parasitic edge damping and 2-D wave propagation effects. This more in-depth analysis will be reported in a future paper.

5 Conclusions

Inverted minority scenarios relevant for the non-activated phase of ITER in H plasmas have been investigated at JET. ^3He minority heating was successfully achieved for $n_{^3\text{He}} / n_e$ below 2% . When $n_{^3\text{He}} / n_e$ was increased above 2% the mode conversion regime dominated. By positioning the conversion layer in the plasma centre, electron temperatures up to 8 keV were obtained using dipole phasing. D minority heating in H plasmas was also tested. This scenario was not successful as the presence of carbon impurity ions led directly to far off-axis fast

wave mode conversion. Preliminary numerical analysis indicates that concentrations as low as 0.5 %, suffice to prevent an efficient absorption at the D minority cyclotron resonance layer. This effect virtually rules out the (D)H scenario for the non-active phase of ITER, leaving (³He)H as the only viable choice. Finally, the code interpretation of the experiments is in progress but computationally challenging due to the presence of short mode-converted waves.

Acknowledgements

This work has been conducted under the European Fusion Development Agreement. It is a pleasure to thank our colleagues who operated the tokamak, the heating systems and the diagnostics during the experiments. The work carried out by the UKAEA personnel was jointly funded by the United Kingdom Engineering and Physical Sciences Research Council and by Euratom. The work of E. Lerche was supported by the EU under an Euratom Intra-European Fellowship.

References

- [1] ITER Physics Basis Editors, ITER Physics Expert Group Chairs and Co-Chairs and ITER Joint Central Team and Physics Integration Unit, Nucl. Fusion **39**, (1999) 12
- [2] Start D.F.H. *et al.*, Nucl. Fusion **39(3)** (1999) 321
- [3] Lamalle P.U. *et al.*, Proc. of the 31st EPS Conf. on Plasma Phys., London, 28 June - 2 July 2004, edited by P. Norreys and H. Hutchinson, European Physical Society, ECA Vol. **28G**, (2004) P-5.165 and http://epsppd.epfl.ch/London/pdf/P5_165.pdf
- [4] Lamalle P.U. *et al.*, Nucl. Fusion **46**, (2006) 391-400
- [5] Stix T.H., “Waves in plasmas”, American Institute of Physics Press, New York, 1992, ISBN 0-88318-859-7
- [6] Stix T.H., Plasma Phys. **14** (1972) 367
- [7] Perkins F.W., Nucl. Fusion **17(6)** (1977) 1197-1224
- [8] Nelson-Melby E. *et al.*, Phys. Rev. Lett. **90(15)** (2003) 155004
- [9] Jaeger E.F. *et al.*, Phys. Rev. Lett. **90(19)** (2003) 195001
- [10] Lin Y. *et al.*, Plasma Phys. and Control. Fusion **45** (2003), 1013-1026]
- [11] Ram A.K. and Bers A., Phys. Fluids B **3** (1991) 10059-10069
- [12] Mantsinen M.J., Mayoral M-L., Van Eester D. *et al.*, Nucl. Fusion **44** (2004) 33-46
- [13] Stix T.H., Nucl. Fusion **15** (1975) 737
- [14] Majeski R., Phillips C.F., Wilson T.R., Phys. Rev. Lett **73** (1994) 2204.
- [15] Bonoli P. *et al.*, Phys. Plasmas **4(5)** (1997) 1774-1782
- [16] Saoutic B. *et al.*, Phys. Rev. Lett. **76(10)** (1996)1647-1650
- [17] Van Eester D. *et al.*, Proc.of 15th Conf. on Radio-Frequency Plasmas, Moran, Wyoming, 19-21 May 2003, edited by Cary B. Forest, American Institut of Physics, Melville, New–York, Vol. **694**, 2004 and <http://proceedings.aip.org/proceedings/confproceed/694.jsp>
- [18] Kaye A. *et al.*, Fusion Eng. and Design **24** (1994) 1

- [19] Wade T.J., Jacquinet J., Bosia G., Sibley A. and Schmid M., Fusion Eng. and Design **24** (1994) 23-46
- [20] Gambier D.J. *et al.*, Nucl. Fusion **30** (1990) 23-24
- [21] Van Eester D., Plasma Phys. and Control. Fusion **42** (2004) 1675-1697.
- [22] De la Luna E. *et al.*, Rev. Sci. Instrum. **75(10)** (2004) 3831-3833
- [23] Mantica P. *et al.*, in Fusion Energy 2002 (Proc. 19th Int. Conf. Lyon, 2002) (Vienna: IAEA) CD-ROM file EX/P1-04 and http://www-pub.iaea.org/MTCD/publications/PDF/csp_019c/START.HTM
- [24] Kiptily V.G. *et al.*, Nucl. Fusion **42** (2002) 999-1007
- [25] Korotkov A.A., Gondhalekar A. and Stuart A.J. 1997, Nuclear Fusion 37 35
- [26] Jarvis O. N. *et al.*, Nucl, Fusion **36(11)** (1996), 1513-1530.
- [27] Ingesson L.C. *et al.*, Nucl. Fusion **38(11)** (1998) 1675-1694.
- [28] Chen L., Vaclavick J. and Hammett G., Nucl. Fusion **28(3)** (1988) 389-398
- [29] Eriksson L.-G. *et al.*, Phys. Rev. Lett. **81(6)** (1998) 1231-1234
- [30] Mantsinen M.J. *et al.*, Phys. Rev. Lett. **89(11)** (2002) 1150004-1
- [31] Hedin J., Hellsten T., Eriksson L.-G. and Johnson T., Nucl. Fusion **42** (2002) 527-540
- [32] Kerner W. *et al.*, Nucl. Fusion **38(9)** (1998) 1315-1332
- [33] Wesson J., "Tokamaks", second edition, Oxford engineering science series 48, Clarendon Press, Oxford, 1997, ISBN 0-19-856293-4
- [34] Lerche E. A. and D. Van Eester, 'Extending the break-in-slope analysis to indirect heating regimes in tokamaks' submitted to Plasma Phys. and Control. Fusion in 2005
- [35] Van Eester D. and Koch R., Plasma Phys. and Control. Fusion **40(11)** (1998) 1949-1976
- [36] Lamalle P.U., LPP-ERM/KMS Lab. Report **101**, Brussels (1994)
- [37] Wright J.C., Bonoli P.T., Brambilla M. *et al.*, Physics of Plasmas **11(5)** (2004) 2473-2479
- [38] Monakhov I., Becoulet A. , Fraboulet D. and Nguyen F., Physics of Plasmas **6(3)** (1999) 885-896

Table

	Antenna A	Antenna B	Antenna C	Antenna D
Frequency (MHz)	37.2	37.3	37.4	36
$R_{ic}({}^3\text{He})$ (m) at 3.6 T	2.94	2.96	2.97	3.06
$R_{ic}({}^3\text{He})$ (m) at 3.3 T	2.64	2.68	2.69	2.78

Table 1: Operating frequencies for the four ICRF antennas and corresponding ${}^3\text{He}$ cyclotron resonance major radii, for $B_t = 3.6$ T and 3.3 T.

	Antenna A	Antenna B	Antenna C	Antenna D
Frequency (MHz)	28.4	28.5	29.3	28.1
$R_{ic}(D)$ (m) at 3.9 T	3.11	3.1	3.02	3.14

Table 2: Operating frequencies for the four ICRF antennas and corresponding D cyclotron resonance major radii, for $B_t = 3.9$ T.

T_e (keV)	$[{}^3\text{He}]$ (%)	$n_\phi = 14$		$n_\phi = 27$	
		P_e (%)	$P_{3\text{He}}$ (%)	P_e (%)	$P_{3\text{He}}$ (%)
3	2	38	7	12	8
5	2	37	12	11	16
8	2	34	20	13	24
3	3.5	36	6	76	2
5	3.5	36	8	72	10
8	3.5	34	12	43	45

Table 3: Total double-pass electron and ${}^3\text{He}$ power heating powers calculated using the TOMCAT simulation code for different plasma target temperatures (3, 5 and 8 keV) and ${}^3\text{He}$ concentrations of 2 and 3.5 %

Figure captions

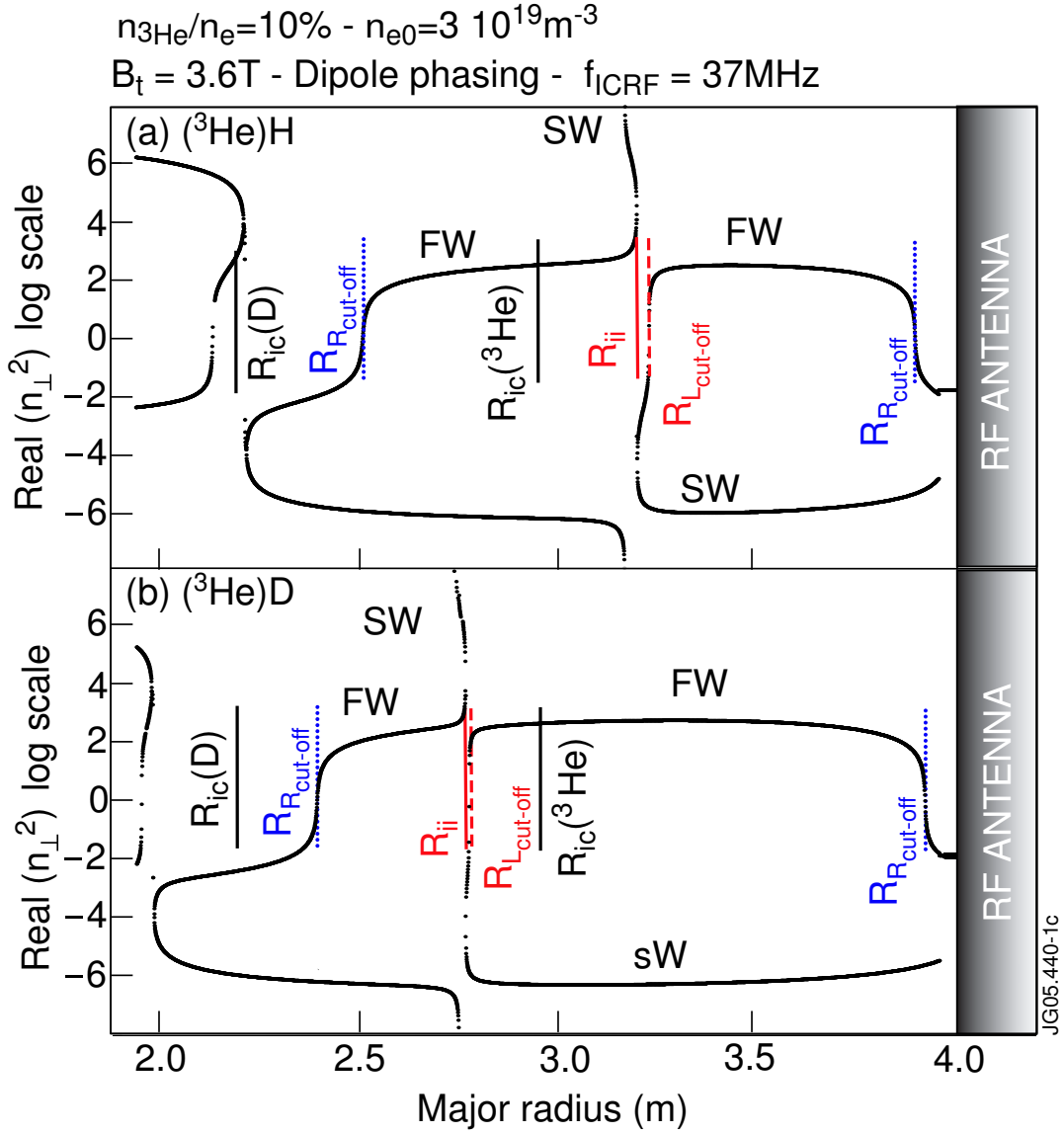


Figure 1. Real part of the square of the perpendicular refractive index obtained from the resolution of the cold plasma dispersion relation. Fast wave (FW) and a short wave (SW) branches are represented. The following radial locations are indicated: FW left-hand cut-off $R_{L\text{cut-off}}$; FW right-hand cut-off $R_{R\text{cut-off}}$; FW resonance R_{ij} ; ion cyclotron resonance R_{ic} . (a) illustrates the inverted MH scenario $(^3\text{He})\text{H}$ and (b) the standard MH scenario $(^3\text{He})\text{D}$. Note: the vertical axis is linear for $|\text{Real}(n_{\perp}^2)| \ll 1$ and logarithmic for $|\text{Real}(n_{\perp}^2)| \gg 1$. In the latter case it corresponds to $\text{sign}(\text{Real}(n_{\perp}^2)) \log(|\text{Real}(n_{\perp}^2)|)$.

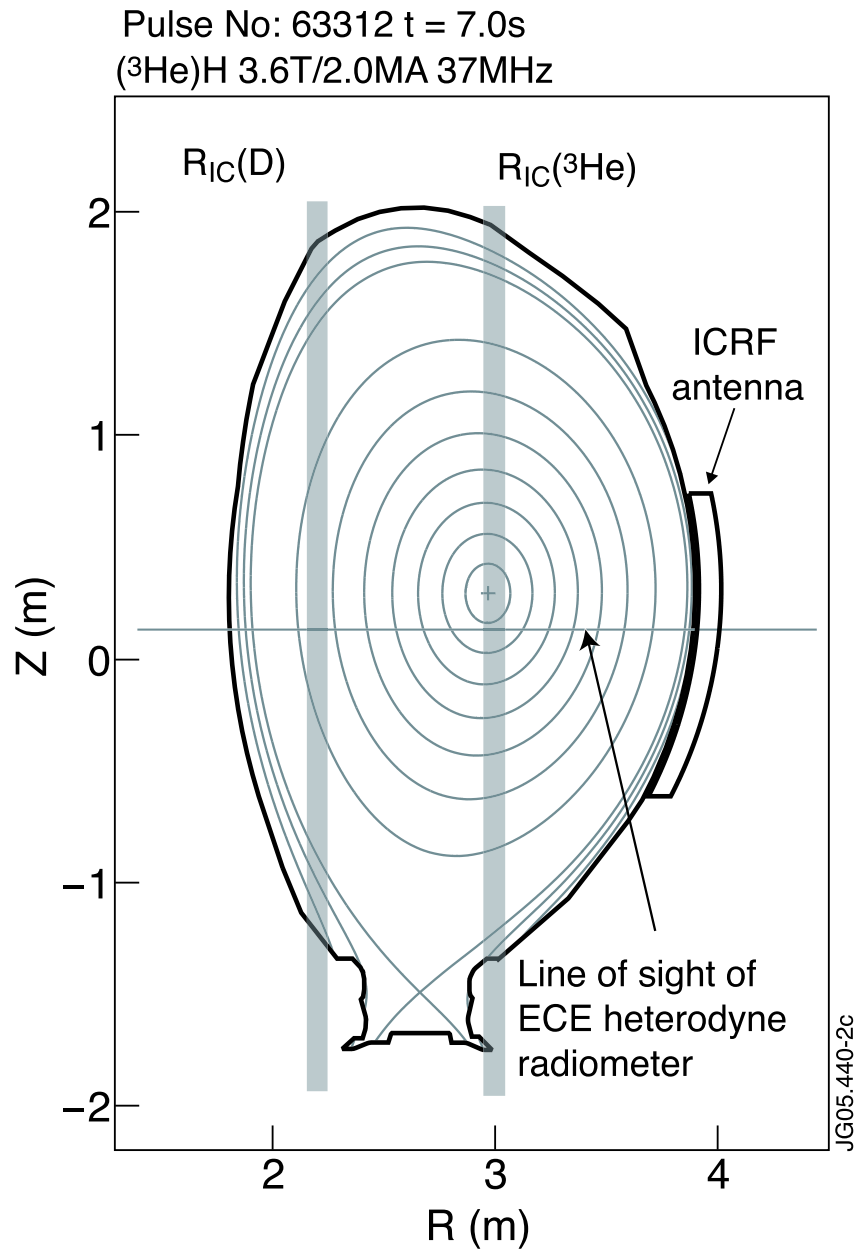


Figure 2. Tokamak poloidal cross-section with locations of the ^3He cyclotron resonance layer $R_{\text{ic}}(^3\text{He})$ and of the D cyclotron resonance layer $R_{\text{ic}}(\text{D})$ for discharge 63312 with $B_t = 3.6$ T and an ICRF frequency of 37 MHz. The ICRF antenna and the line of sight for the ECE electron temperature measurements are also shown.

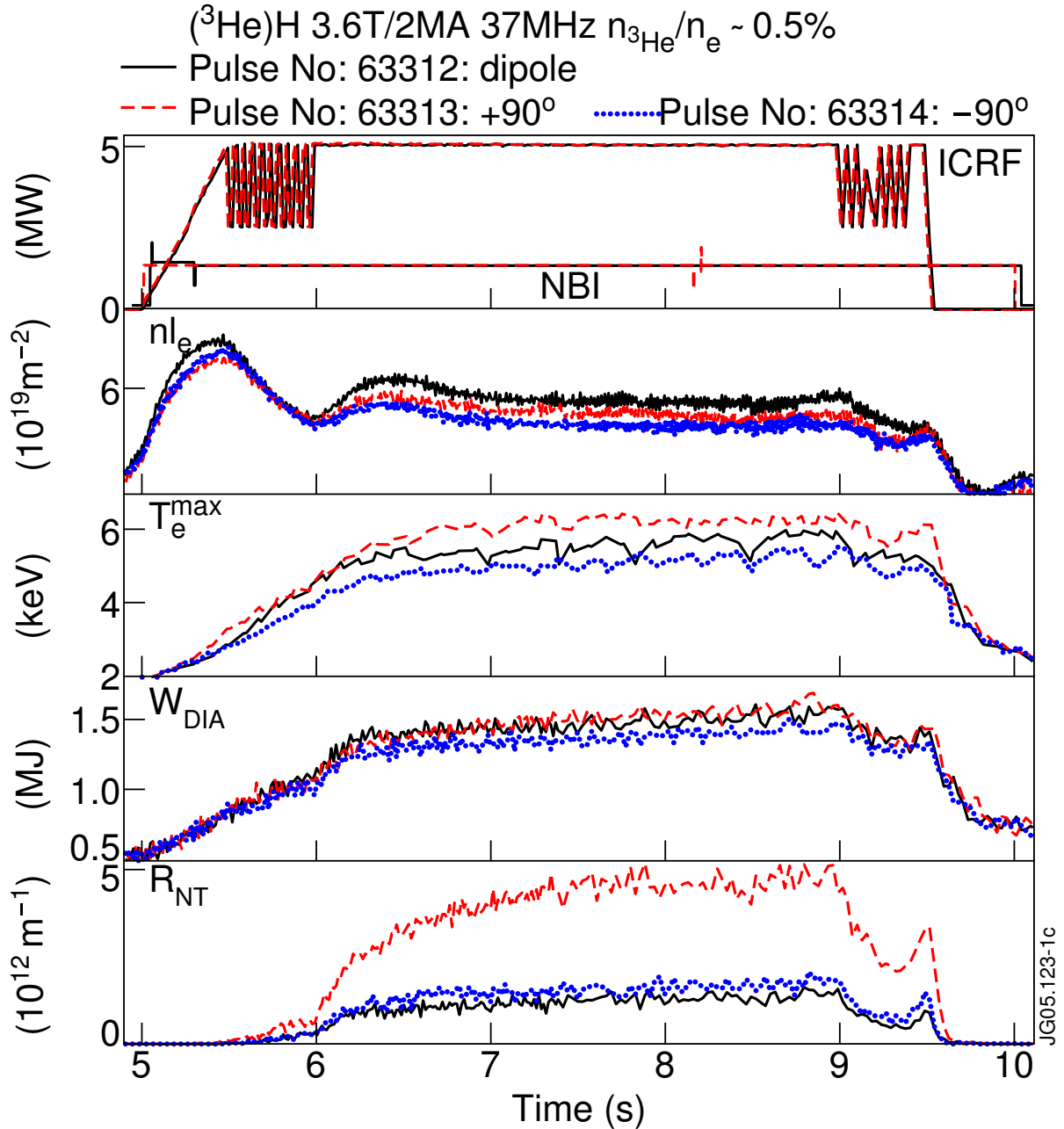


Figure 3. Time evolution of the ICRF and NBI power (H beams), central line integrated density from the far infrared interferometer diagnostic (the central density n_{e0} , from LIDAR Thomson Scattering, was $n_{e0} = 3 \cdot 10^{19} \text{ m}^{-3}$ for pulses 63312 and 63314; LIDAR data were not available for the pulse 63313), maximum electron temperature from the ECE Michelson interferometer diagnostic, plasma diamagnetic stored energy and neutron rate from $^9\text{Be}(^3\text{He},n)^{11}\text{C}$ reaction. Three discharges are represented for different ICRF antenna phasings: dipole, $+90^\circ$ and -90° .

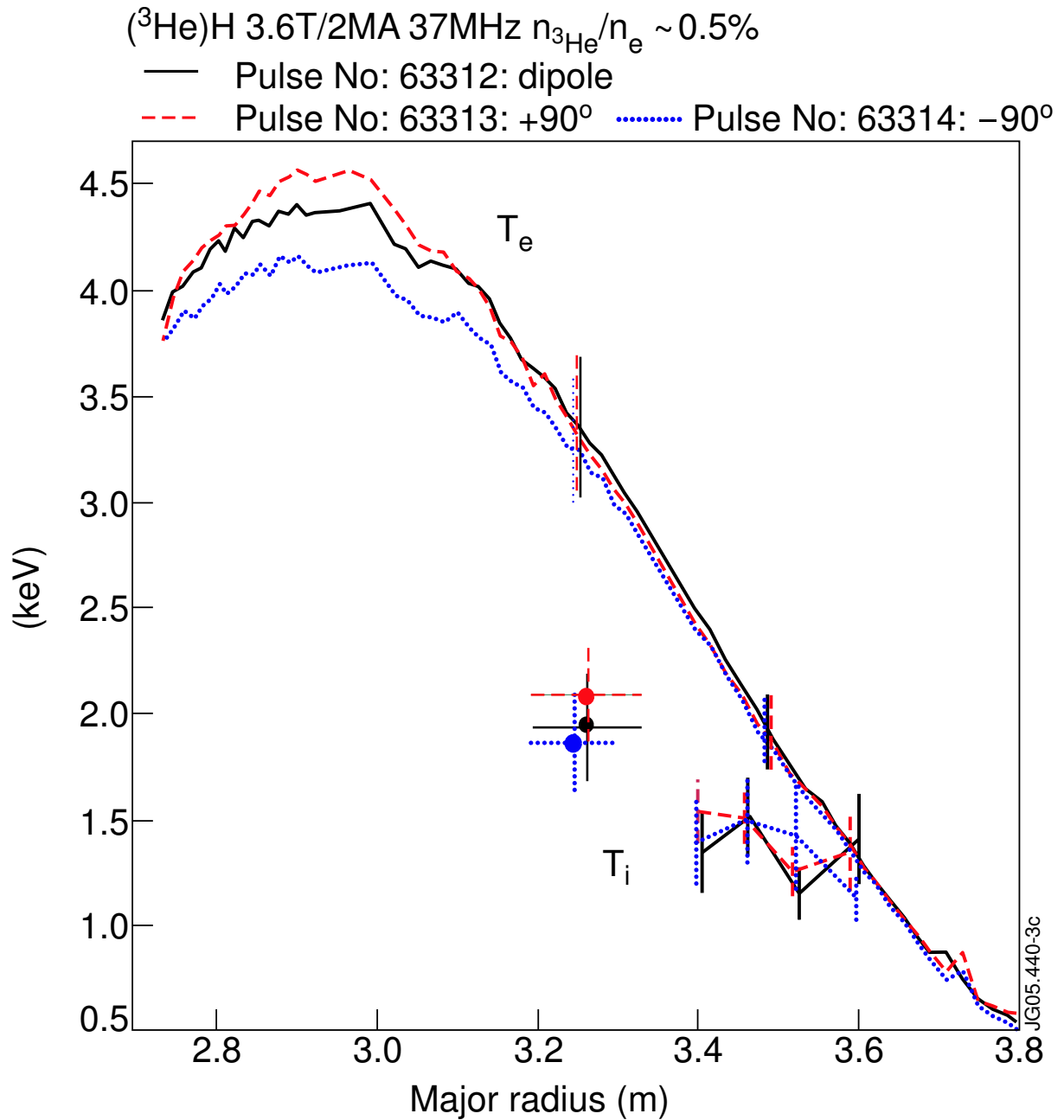


Figure 4. Radial profiles of the electron temperature (from the ECE heterodyne radiometer at around 0.17 m below the magnetic axis). The ion temperature data at $R = 3.25$ m are measured with a X-ray crystal spectrometer. The ion temperature profiles at the plasma edge are measured by edge charge exchange recombination spectroscopy.

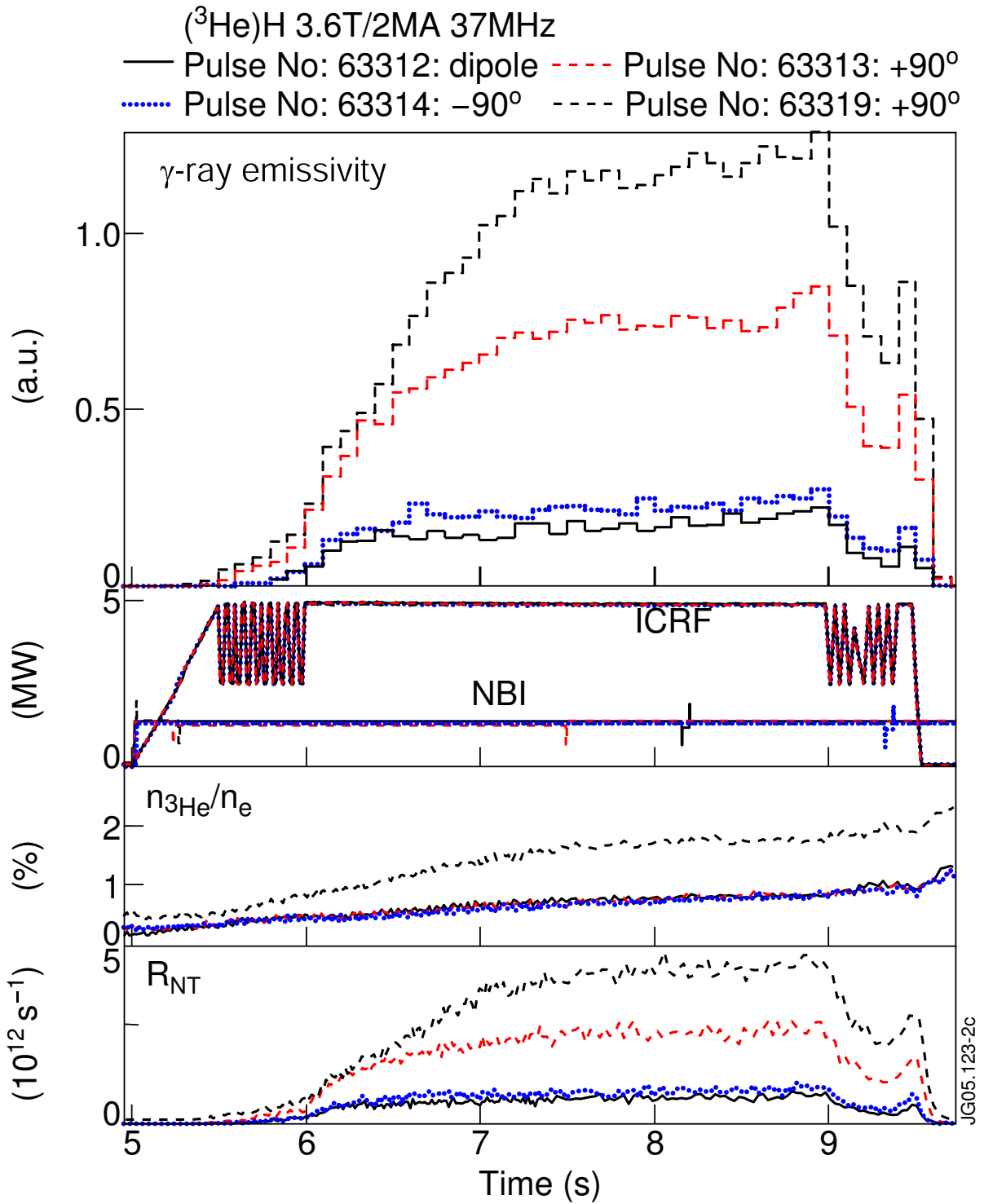


Figure 5. Time evolution of the γ -ray emissivity, ICRF and NBI power, ^3He concentration and neutron rate for pulses 63312 (dipole), 63313(+90°), 63314 (-90°) with ^3He concentration below 1 % and pulse 63319 (+90°) with ^3He concentration up to 1.8 %.

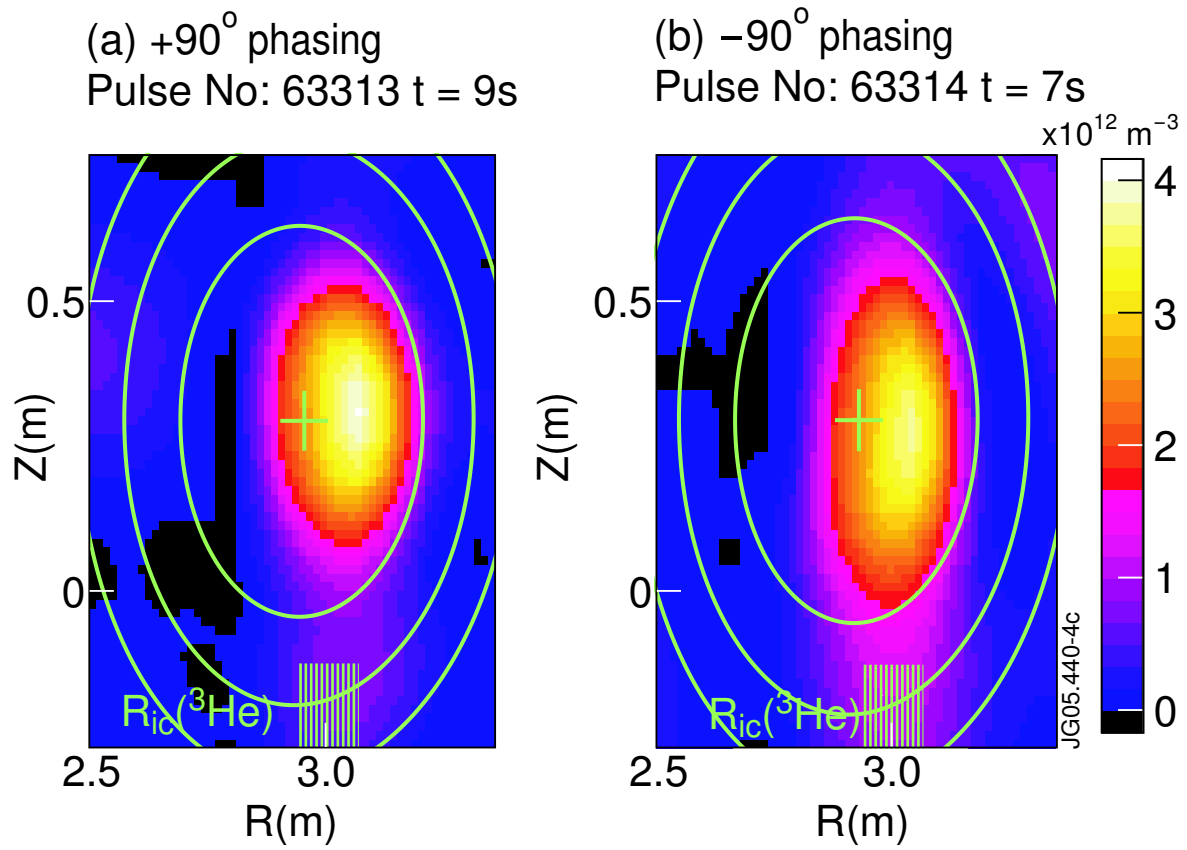


Figure 6. γ -ray emission profiles (normalised to the peak value) for a $+90^\circ$ phasing case (pulse 63313) and a -90° phasing case (pulse 63314). A number of flux surfaces are shown in green; a green cross indicates the magnetic axis. The ^3He ion cyclotron resonance layer $R_{ic}(^3\text{He})$ is also represented.

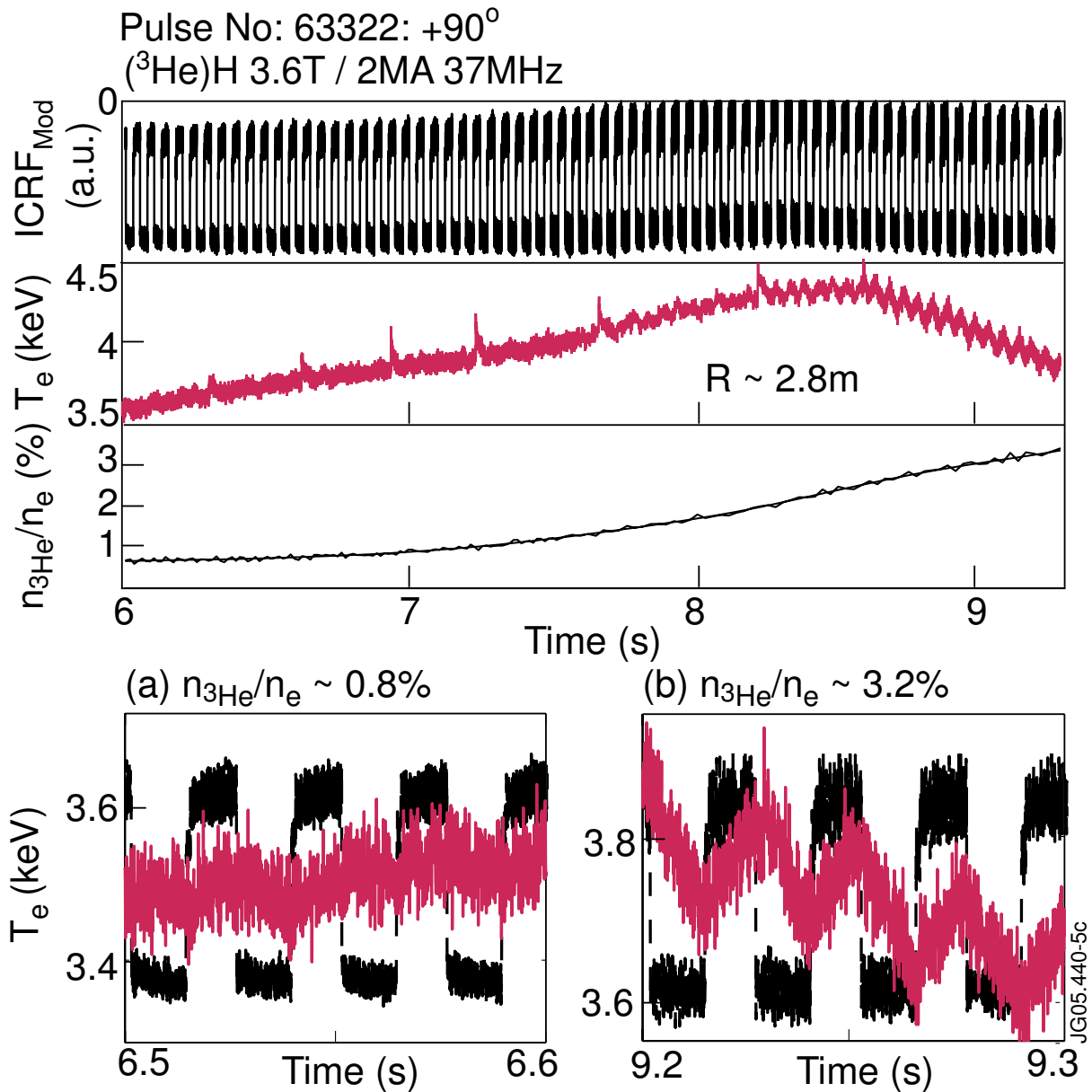


Figure 7. Time evolution of the ICRF power modulation, electron temperature at $R = 2.8$ m from ECE measurements and ^3He concentration for the pulse 63322 (+90° phasing). Zooms on the electron temperature response to the ICRF power modulation are also represented for (a) $n_{3\text{He}}/n_e \approx 0.8\%$ and (b) $n_{3\text{He}}/n_e \approx 3.2\%$.

(³He)H 3.6T/2MA 37MHz +90°

— Pulse No: 63319 - - - Pulse No: 63320

..... Pulse No: 63324

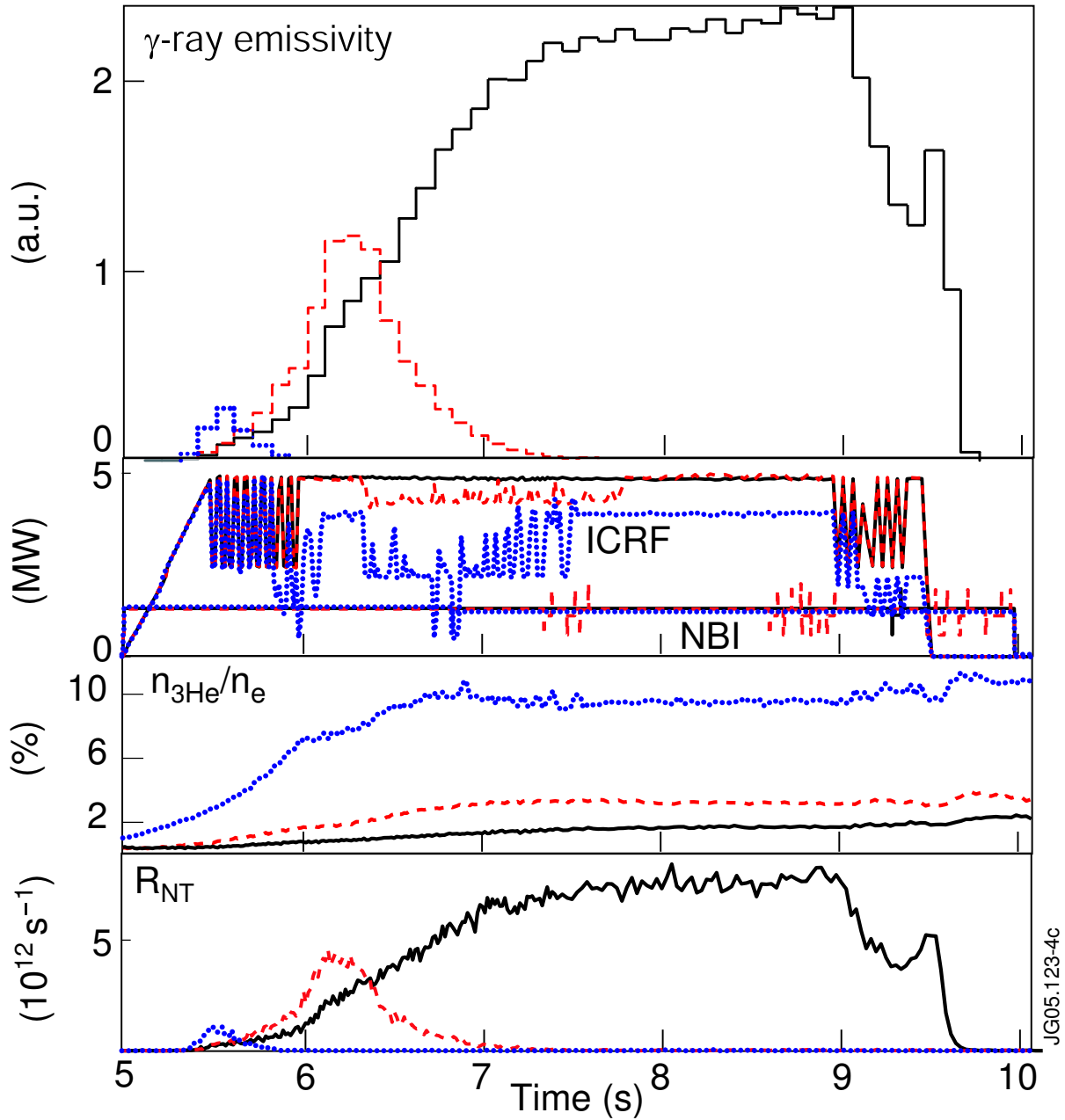


Figure 8. Time evolution of the γ -ray emissivity, ICRF and NBI power, ³He concentration and neutron rate for pulses 63319, 63320, 63324.

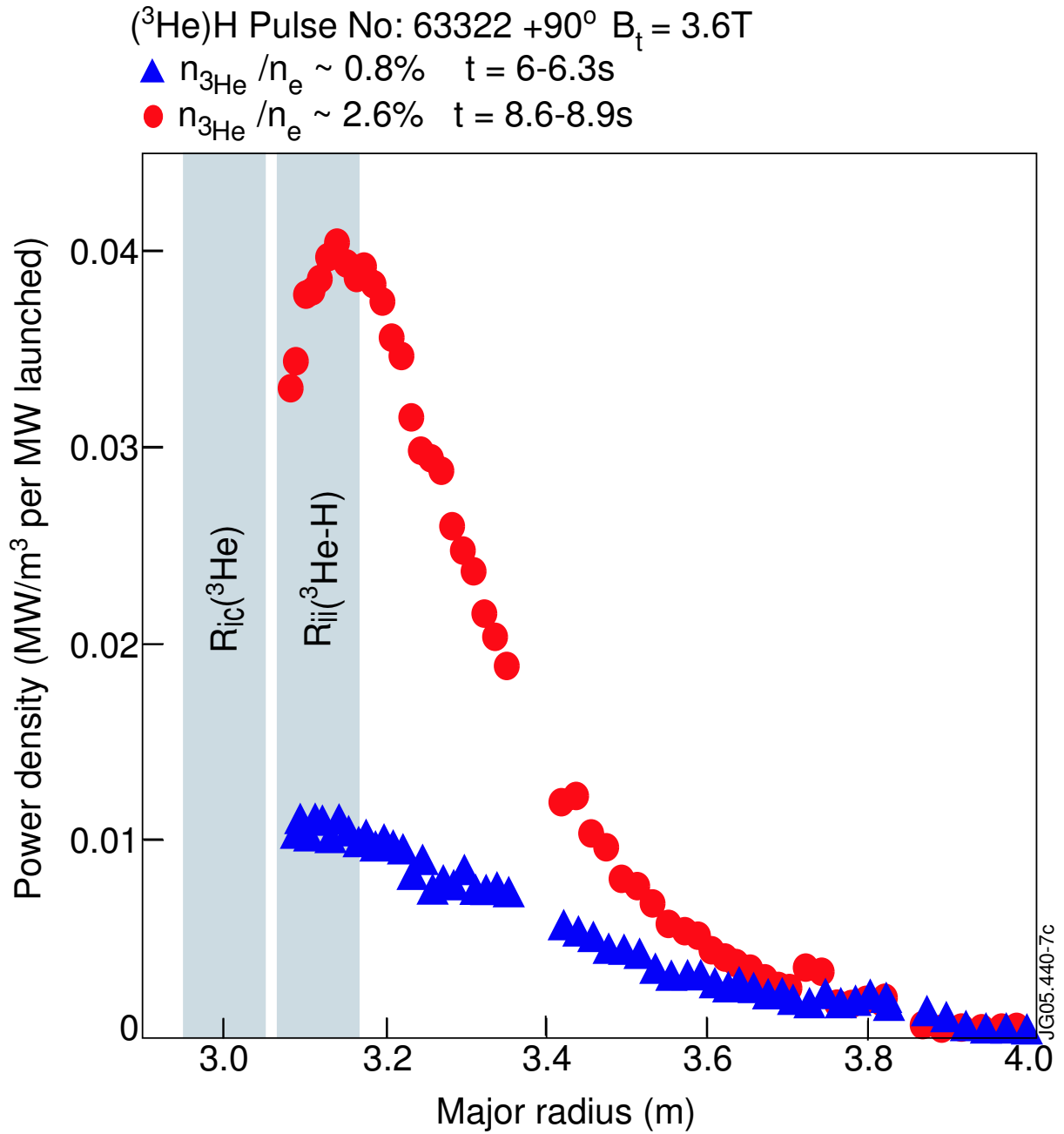


Figure 10. Electron deposition profiles from upgraded BIS analysis at two different ³He concentrations for the pulse 63322. The triangles correspond to $n_{3\text{He}}/n_e \approx 0.8\%$ (MH regime). The dots correspond to $n_{3\text{He}}/n_e \approx 2.6\%$ (MC regime). The ³He cyclotron resonance layer R_{ic}(³He) and the ³He-H hybrid layer R_{ii}(³He-H) are also represented.

$(^3\text{He})\text{H}$ Pulse No: 63322 +90° $B_t = 3.6\text{T}$

$t = 6 - 6.3\text{s}$ $n_{^3\text{He}}/n_e \sim 0.8\%$

○ standard BIS -> direct electron heating

▲ new BIS ■ FFT $n=1$ - > direct + indirect electron heating

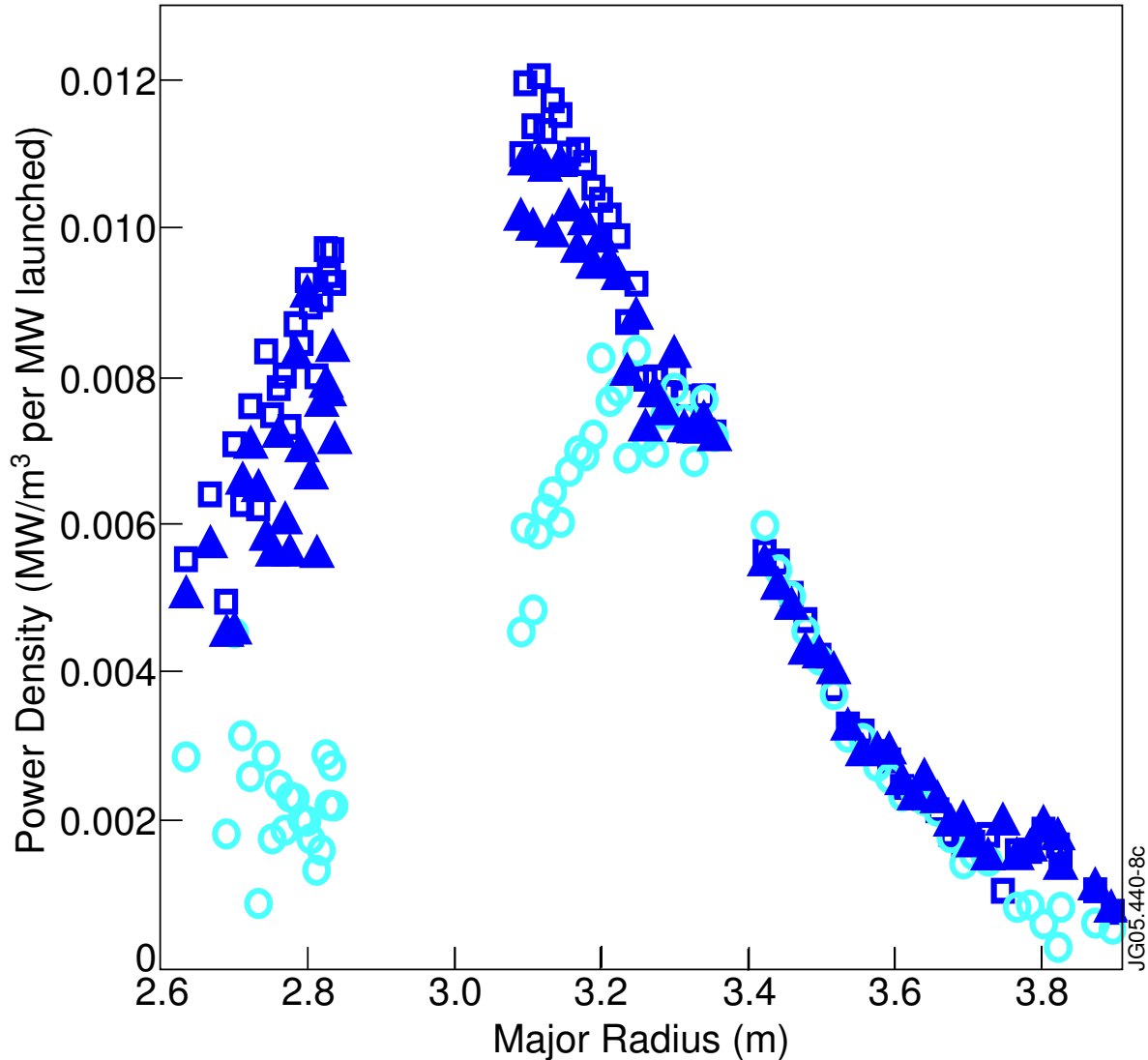


Figure 11. Electron deposition profiles from three different methods: standard BIS, new BIS and FFT. The new BIS analysis takes into account delays in the electron temperature response to the ICRF power modulation. The FFT and the new BIS method accounts for direct and indirect electron heating. The standard BIS method accounts for direct electron heating only. Disagreement between the FFT (or the new BIS) and the standard BIS methods indicates indirect electron heating at the location of the disagreement.

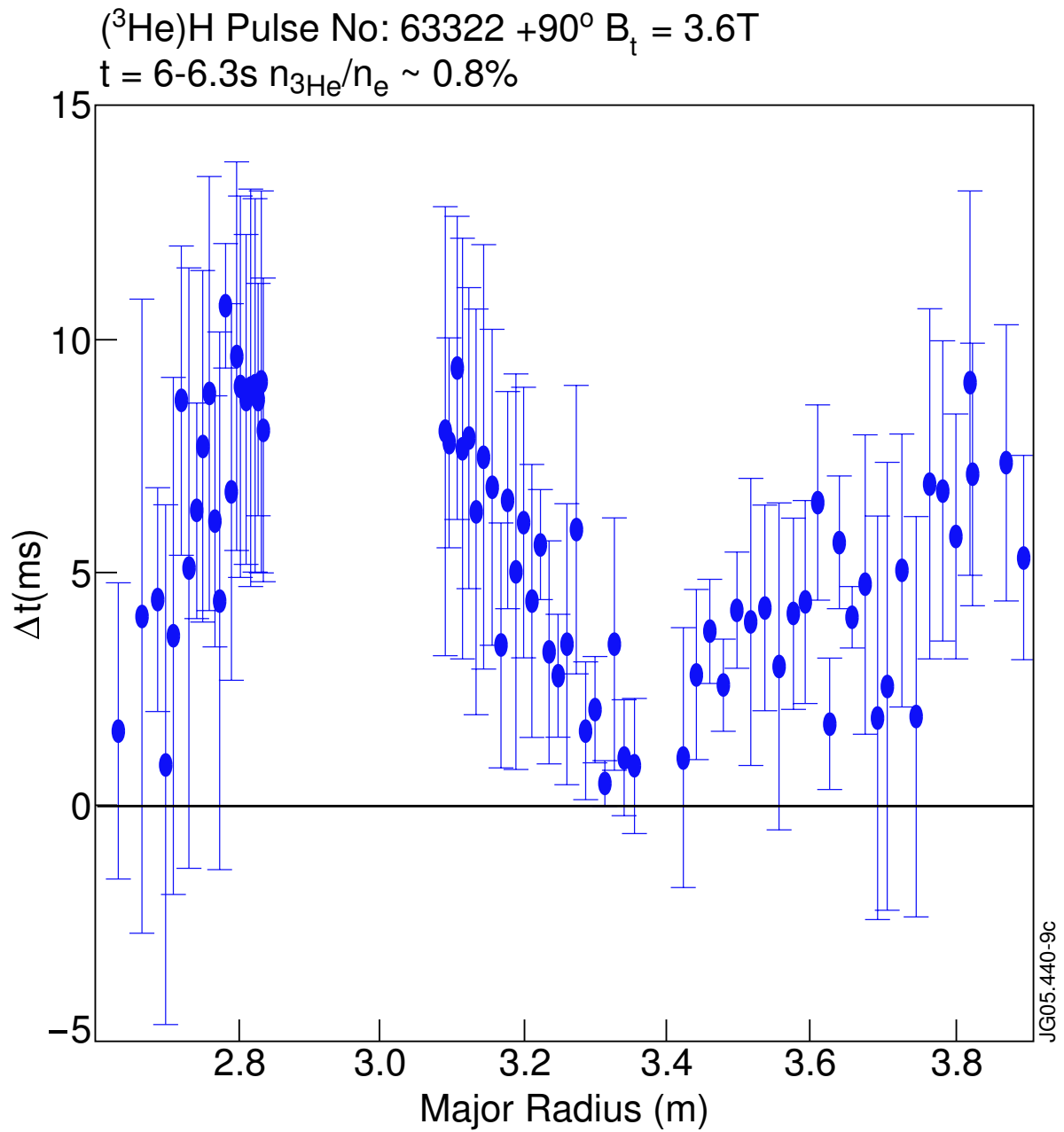


Figure 12. Time delay between the electron temperature response and the ICRF power modulation obtained with the new BIS method.

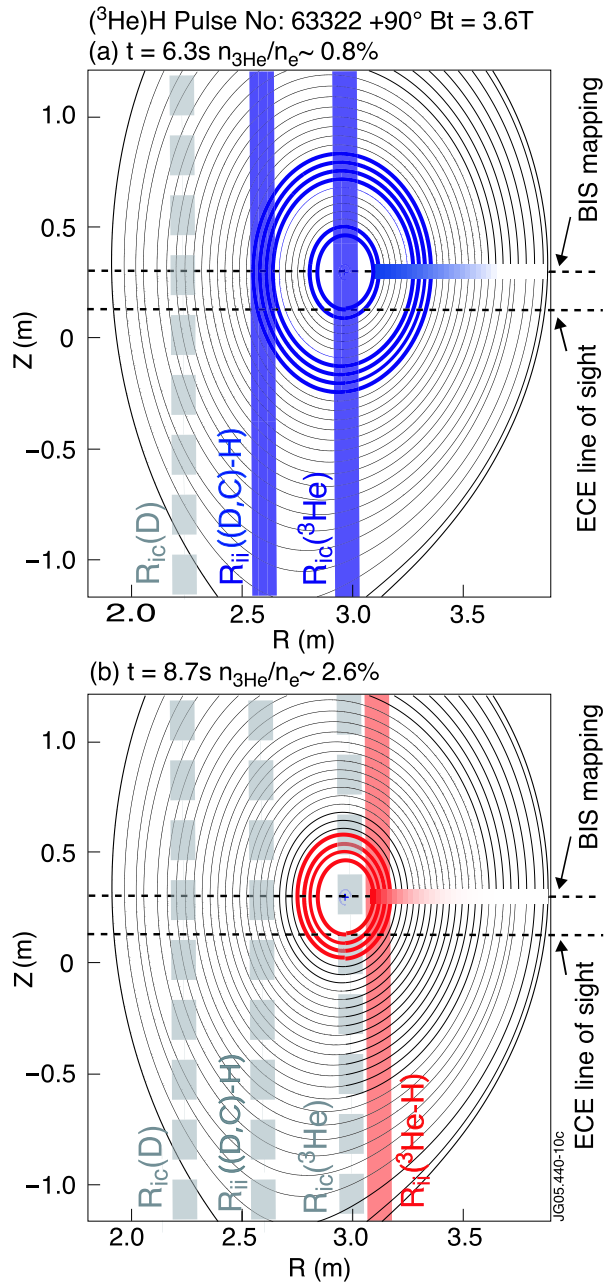


Figure 13. Tokamak poloidal section with locations of the ^3He cyclotron resonance $R_{ic}(^3\text{He})$, the D cyclotron resonance $R_{ic}(\text{D})$, the ^3He -H hybrid layer $R_{ii}(^3\text{He}-\text{H})$ and the (D,C)-H hybrid layer $R_{ii}(\text{D,C})-\text{H}$. One assume 2 % of D, 2 % of C , $B_t = 3.6$ T and an ICRF frequency of 37 MHz. The line-of sight for the ECE electron temperature measurements are also shown as well as the Z position at which the BIS profiles are mapped. (a) is for $n_{3\text{He}}/n_e \approx 0.8$ % and (b) is for $n_{3\text{He}}/n_e \approx 2.6$ %.

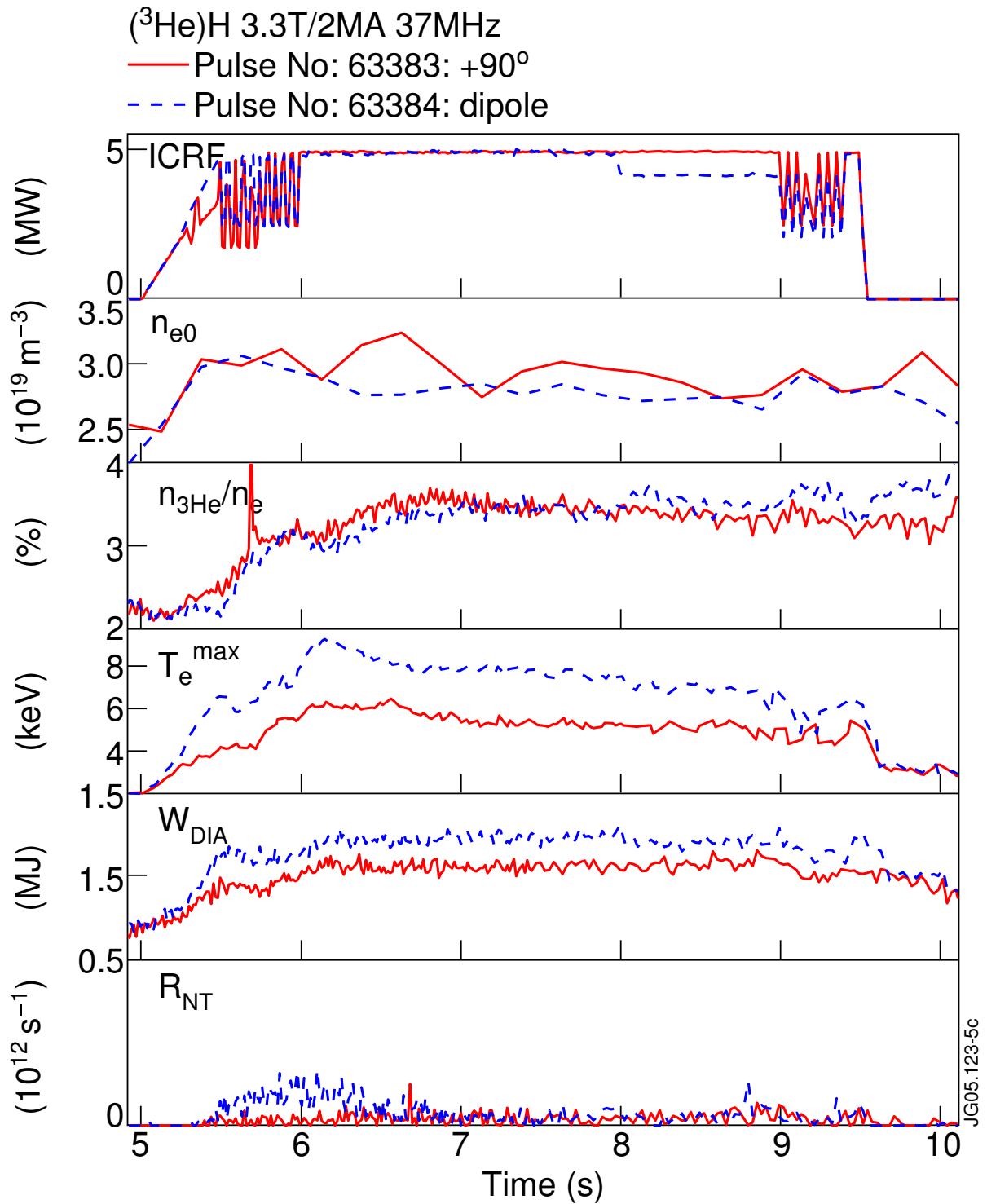


Figure 14. Time evolution of the ICRF power, central electron density from LIDAR Thomson scattering, ^3He concentration, maximum electron temperature from the ECE Michelson interferometer, plasma diamagnetic stored energy and neutron rate from $^9\text{Be}(^3\text{He},n)^{11}\text{C}$ reaction. Two discharges are presented for dipole and +90° ICRF wave phasing.

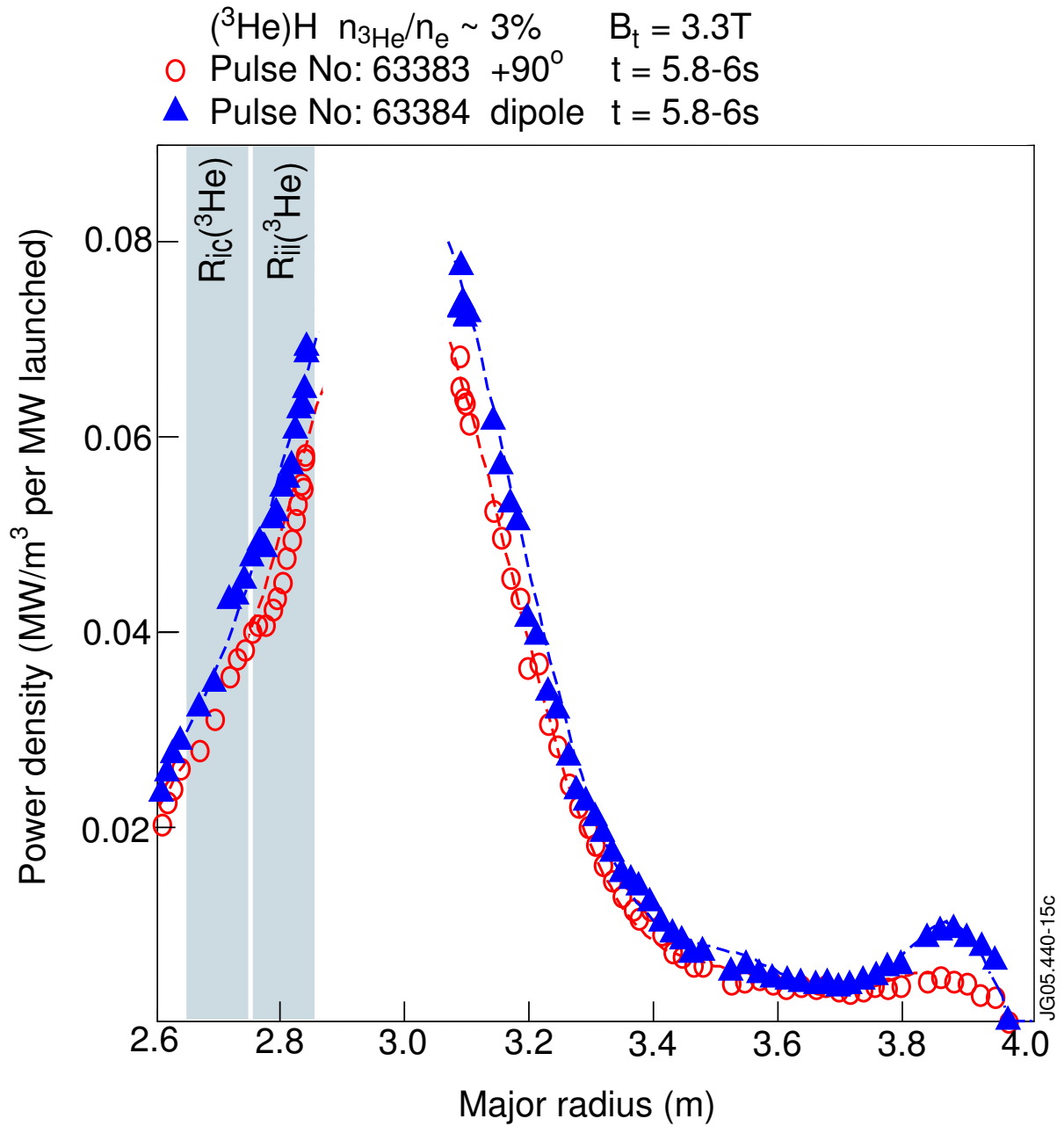


Figure 15. Direct electron deposition profiles from new break-in-slope analysis [34] for different pulses with similar ^3He concentration but different ICRF wave phasings.

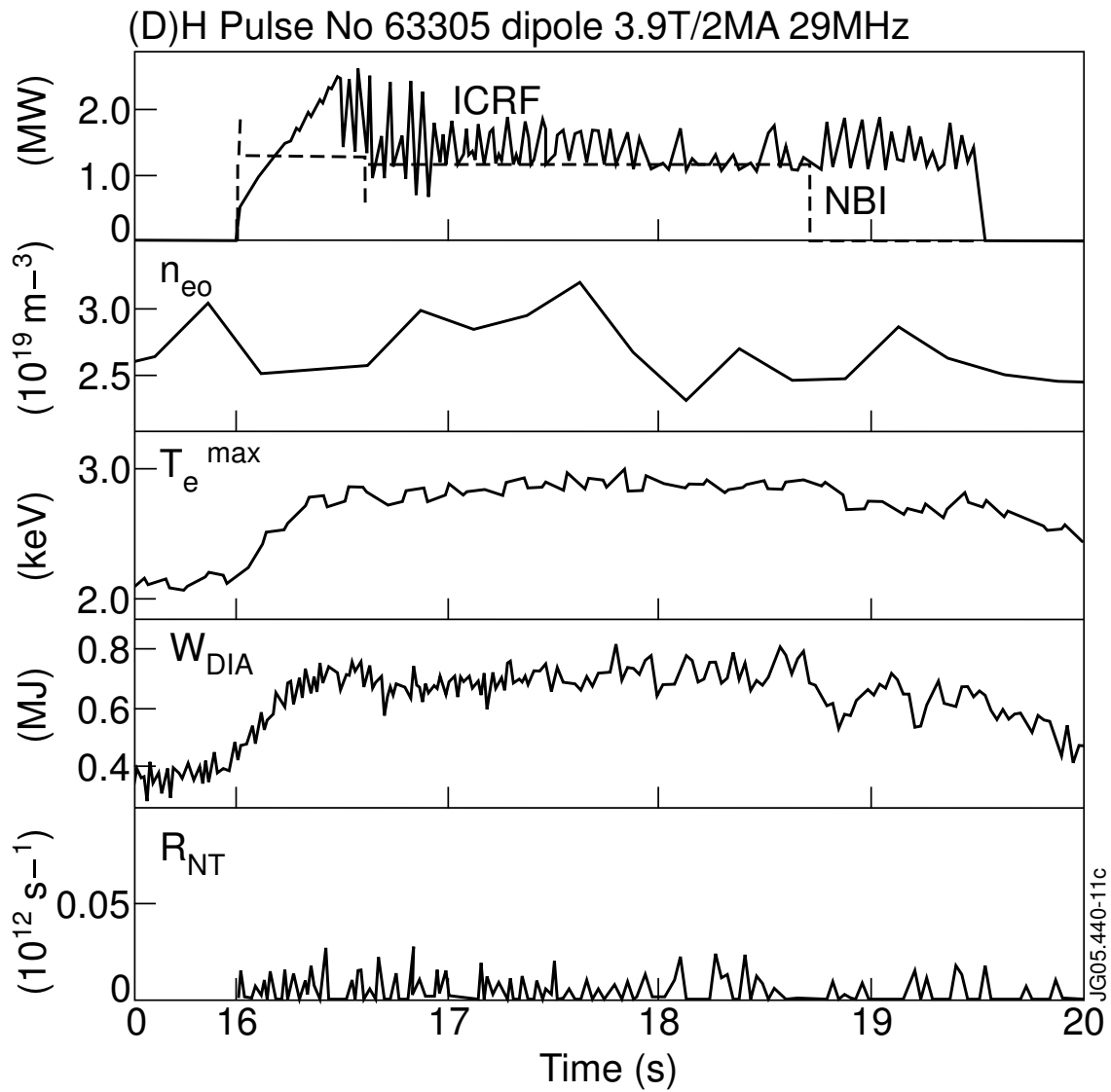


Figure 16. Time evolution of the ICRF power, NBI power (H beams), central electron density from LIDAR Thomson scattering, maximum electron temperature from the ECE Michelson interferometer, plasma diamagnetic stored energy and neutron rate.

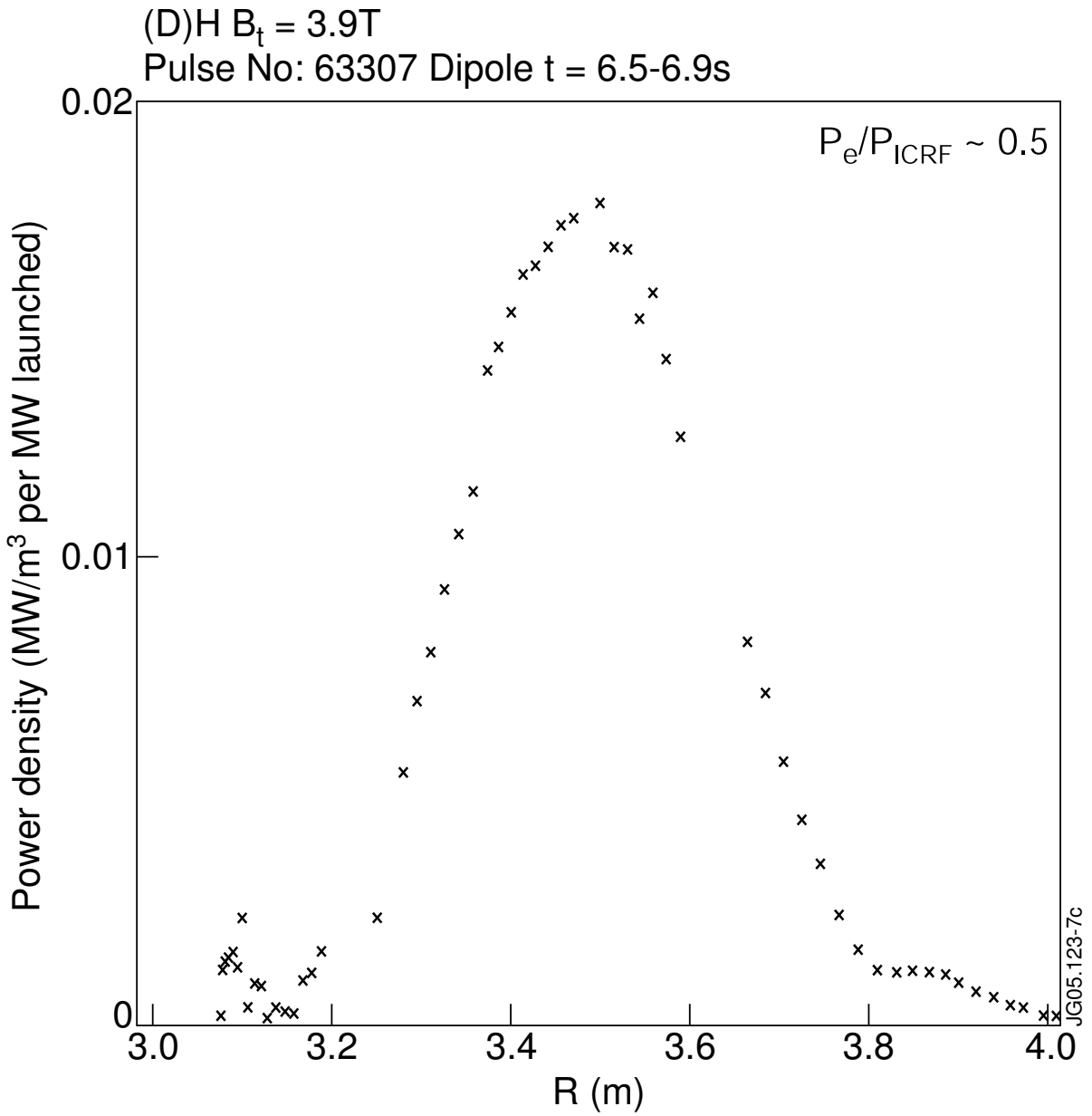


Figure 17. Typical direct electron deposition profile from BIS analysis in the (D)H experiments.

(D)H $B_t = 3.9T$
 $n_{e0} = 3 \cdot 10^{19} m^{-3}$ - Dipole phasing - $f_{ICRF} = 29MHz$

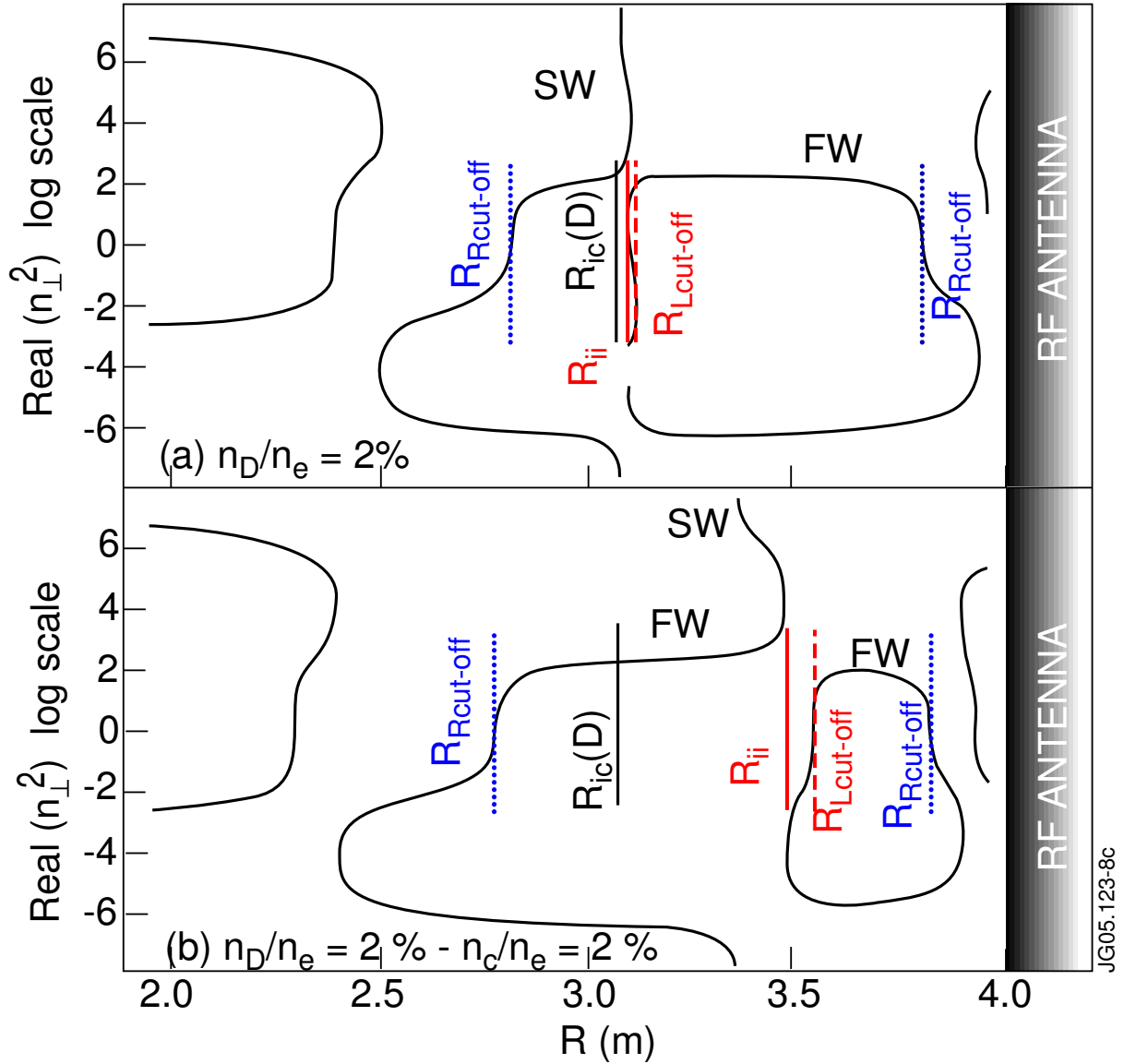


Figure 18. Real part of the square of the perpendicular refractive index obtained from the resolution of the cold plasma dispersion relation.. Fast wave (FW) and slow wave (SW) branches are represented. The following radial locations are indicated: FW left cut-off $R_{Lcut-off}$; FW right cut-off $R_{Rcut-off}$; FW resonance R_{ii} ; D cyclotron resonance R_{ic} . Two cases are plotted: (a) with 2 % of D and (b) with 2 % of C and 2 % of D. Note: the vertical axis is linear for $|\text{Real}(n_{\perp}^2)| \ll 1$ and logarithmic for $|\text{Real}(n_{\perp}^2)| \gg 1$. In the latter case its corresponds to $\text{sign}(\text{Real}(n_{\perp}^2)) \log(|\text{Real}(n_{\perp}^2)|)$.

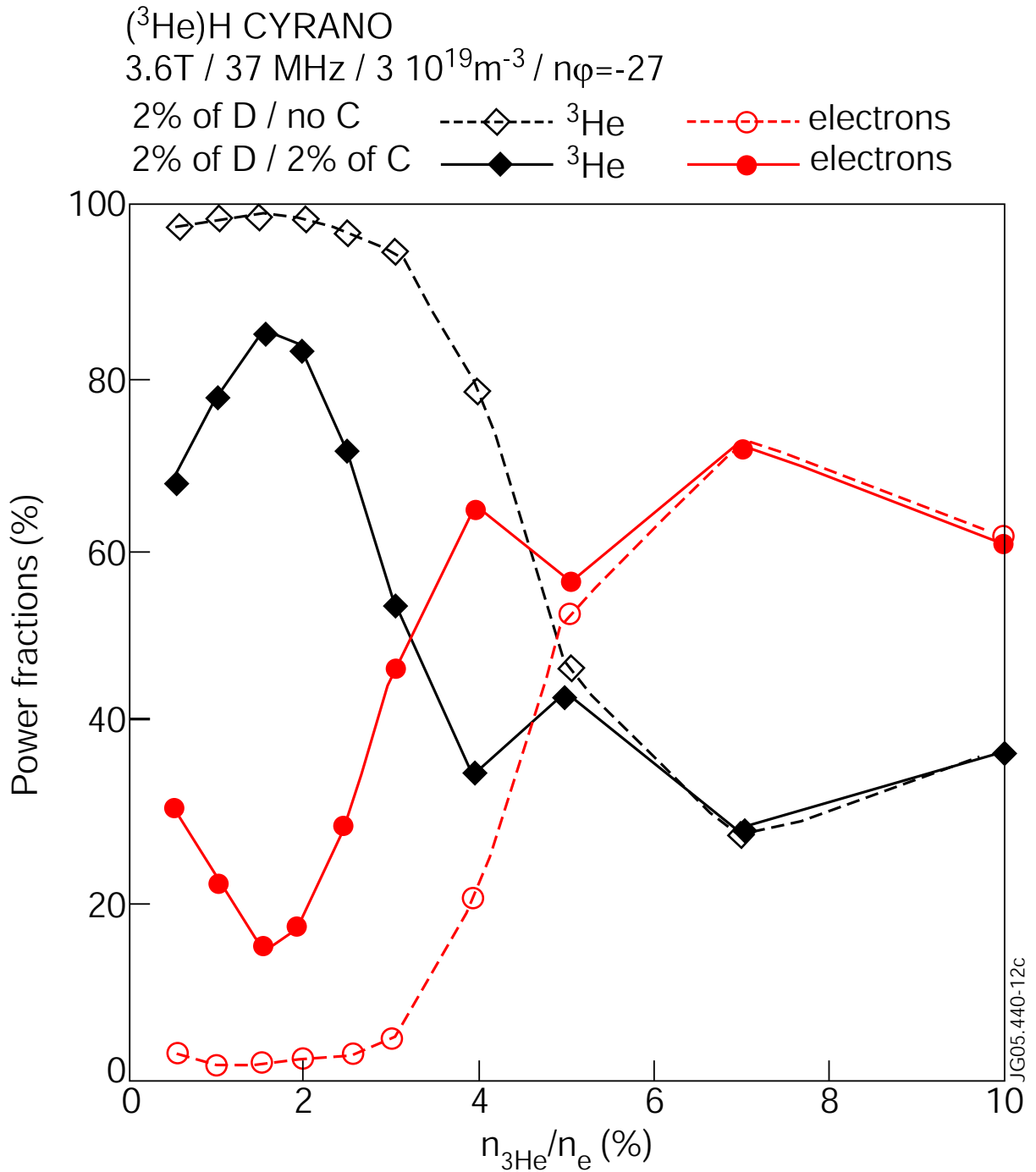


Figure 19. CYRANO simulations of ³He ions heating in H plasmas: ICRF power directly absorbed by the electrons and the ³He ions as a function of the ³He concentration. The unfilled symbols correspond to simulations without C and the filled symbols to simulations with 2% of C.

TOMCAT (^3He)H $B_t = 3.3\text{T}$
 $n_{^3\text{He}}/n_e = 2\%$ $-n_C/n_e = 2\%$ $-n_{e0} = 3 \cdot 10^{19}\text{m}^{-3}$ $-f_{\text{ICRF}} = 37\text{MHz}$

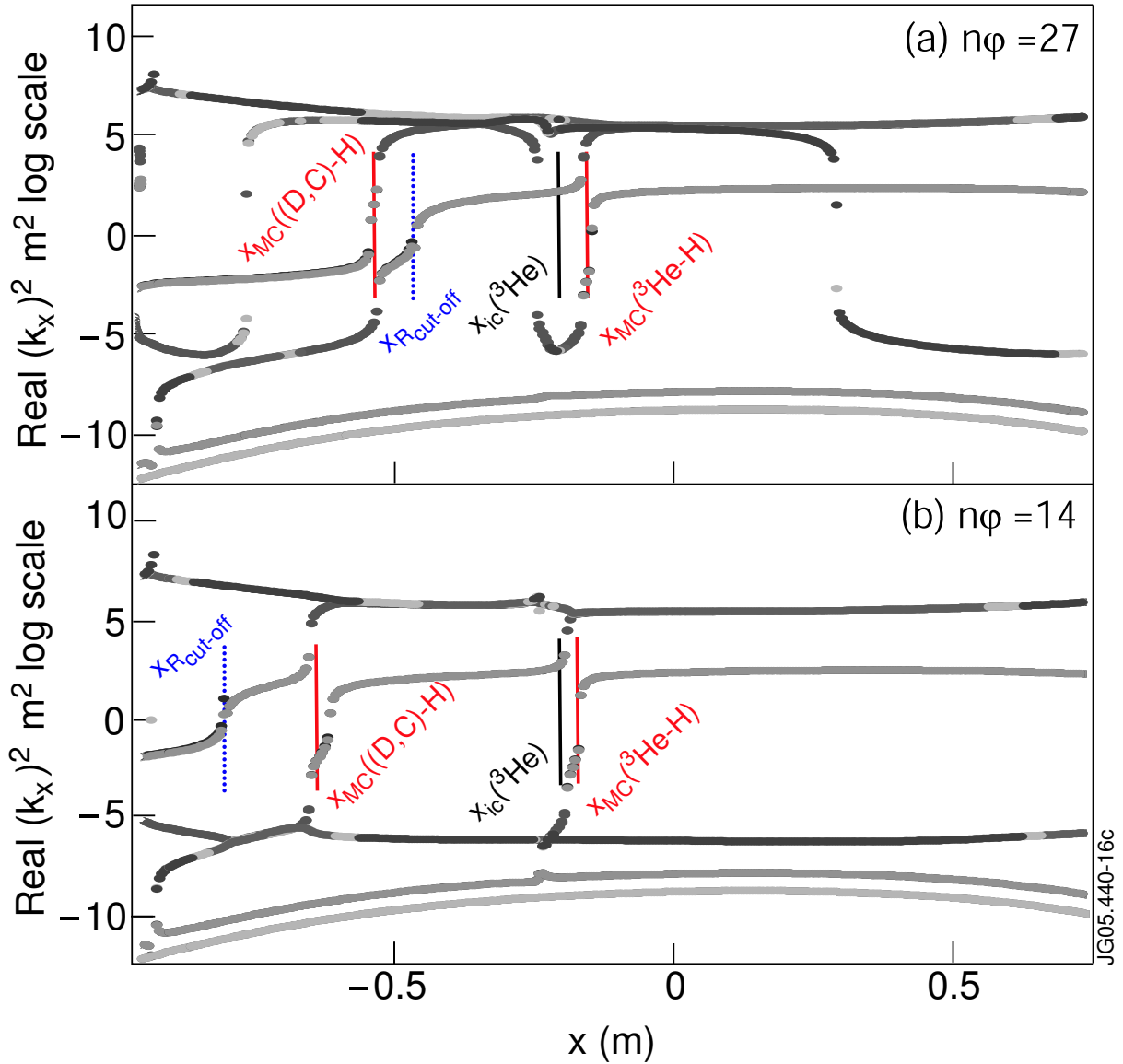


Figure 20. TOMCAT simulations of ^3He ions heating in H plasmas: real part of the square of refractive index obtained from plasma dispersion relation with a target temperature of 3 keV . The following locations are indicated: FW right-hand cut-off $x_{\text{Rcut-off}}$; MC layer associated with the ^3He and H ions $x_{\text{MC}}(^3\text{He-H})$; MC layer associated with the (D,C) and H ions $x_{\text{MC}}((\text{C,D})-\text{H})$; ^3He ion cyclotron resonance $x_{\text{ic}}(^3\text{He})$. Two cases are plotted: (a) dominant mode of dipole phasing $n_\phi = 27$ and (b) dominant mode of $+90^\circ$ phasing $n_\phi = 14$.

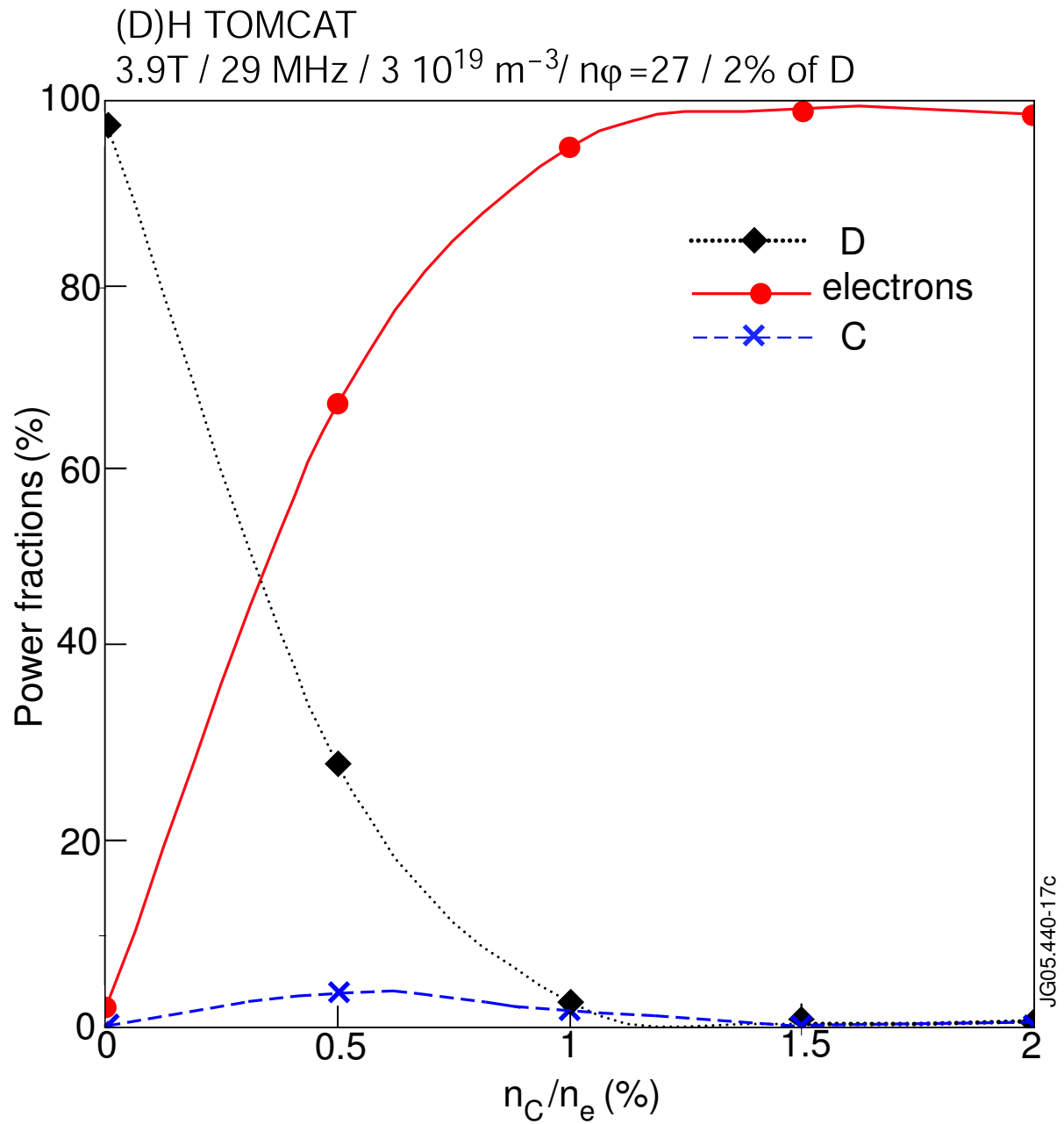


Figure 21. TOMCAT simulations of D ions heating in H plasmas : ICRF power directly absorbed by the electrons and the D ions as a function of the C concentration.